日本原子力研究開発機構

# Reports on JAEA's Reimei Research Program

## April 1, 2013 – March 31, 2015

(Ed.) Yuichiro NAGAME

Advanced Science Research Center
Sector of Nuclear Science Research

JAEA-Review

Reports on JAEA's Reimei Research Program
April 1, 2013 – March 31, 2015

(Ed.) Yuichiro NAGAME

Advanced Science Research Center
Sector of Nuclear Science Research
Japan Atomic Energy Agency
Tokai-mura, Naka-gun, Ibaraki-ken

The Reimei (Dawn) Research Program is conducted based on public application to encourage original and/or unique ideas in the field of new frontier research on atomic energy sciences. Candidates for the offering have been extended beyond the country since the fiscal year of 2010. The seven research subjects were accepted in the fiscal year of 2013, and six of them were carried out in the fiscal year of 2014, too. They have achieved substantial progress through the effective international collaboration.

The summaries of these research subjects are compiled in this report. We hope that new frontier research projects will be developed through the present Reimei Research Program.

平成 25-26 年度黎明研究成果報告集

日本原子力研究開発機構
原子力科学研究部門　先端基礎研究センター
（編）　永目　諭一郎

　原子力科学の分野で革新的な原理や現象の発見を目指す先端基礎研究を対象として、研究テーマを原子力機構外から公募する黎明研究制度が平成 18 年度から新たに発足した。平成 22 年度からは応募対象を国外にも広げ、国際共同研究へと発展させている。平成 25 年度は 7 件新規に採択され、そのうち 6 件が平成 26 年度も継続し、先端基礎研究センターとの共同研究として実施された。継続課題の研究は、大きな進展を遂げており、国際共同研究による研究交流が効果的に機能している。
　本報告書は、黎明研究から多くの基礎・基盤研究が進展する一助とするため、黎明研究の実施者より提出された成果報告書をまとめ、公表するものである。

# Contents

# 目次

# 1. Spin orbit coupling and spin mechanics

Yaroslav Blanter[1], Gerrit E.W. Bauer[1,2], Timothy Ziman[3] and Michiyasu Mori[4]

[1]Kavli Institute of NanoScience, Delft University of Technology, Delft, The Netherlands

[2]Institute for Materials Research & WPI-AIMR, Sendai, Japan

[3]Institut Laue Langevin and CNRS, 6 rue Jules Horowitz, 38042 Grenoble, France

[4]Advanced Science Research Center, JAEA, Tokai, Ibaraki 319-1195, Japan

Abstract

We study theoretically the effects of spin orbit coupling on electronic transport as well as the interactions between spin, lattice, and electromagnetic waves in bulk materials and at interfaces.

## 1. Research objectives

The bosonic excitations of the magnetic order parameter and the crystal lattice are known as magnons and phonons, respectively. They interact with each other via the magnetoelastic coupling, which implies that they both can be excited electrically or thermally in magnetic insulators by heavy metallic contacts.

An essential ingredient of the coupling between spin and mechanical angular momentum including the magnetoelastic coupling is the spin-orbit interaction. Strong spin-orbit interaction as is evident in recent hot topics in spintronics, e.g. in the spin Hall effect and spin-orbit torques, implies an enhanced coupling to the lattice but has not attracted much attention yet. The spin-orbit interaction is relativistic corrections and important in heavier atoms such as platinum, but the detailed electronic structure and the nature of impurities play essential roles as well. It is important, then to understand fully situations in which spin orbit interaction is enhanced and this is the common element of investigations reported here.

We pursued the theoretical investigation in three main directions, viz. coupling of magnetic and structural excitations in ferromagnetic insulators, the role of spin-orbit coupling in phenomenological as well as microscopic calculations of the anomalous and spin Hall Effects, as well as spin-dependent scattering from Muonium. In each case the calculations have been carried out in conjunction with experimentalists, at the ISSP (Kashiwa), KEK (Tsukuba), ILL (Grenoble), and Tohoku University (Sendai).

## 2. Research contents

This research proposal is a collaboration of two different research communities that find a common denominator in the projects carried out at the ASRC. On one hand the Grenoble group is interested in the microscopic mechanism that governs the effects of the spin orbit interaction on transport while the Delft/Tohoku group is interested in its phenomenology as well the consequences of driving the lattice via the spin orbit interaction and vice versa. The ASRC team is interested in all topics, integrating spin electronics [1], caloritronics [2], and mechanics [3].

## 3. Research results

### 3.1 Hybrid systems

(1) Strong magnon-phonon coupling: We model the injection of elastic waves into a ferromagnetic film (F) by a non-magnetic transducer (N) [4]. We compare the configurations in which the magnetization is (a) parallel (b) normal to the wave propagation (Fig. 1-1). The lack of axial symmetry in the former results in the emergence of evanescent interface states. We compute the energy-flux transmission across the N|F interface and sound-induced magnetization dynamics in the ferromagnet (Fig. 1-2). We predict acoustically induced pumping of spin current into a metal contact attached to F as shown in the figure in which the spin pumping signals are expressed as the ratio between the squared cone angle of induced magnetic precession at the interface that is proportional to the pumped spin current and the invested acoustic energy flux for a magnetic film with finite thickness and reflecting as well as damped boundary conditions on the opposite side of the actuator.

(2) Strong magnon-photon coupling: In analogy of the magnon-phonon system we formulate a scattering theory for the magnon-photon system to study magnetic films in microwave
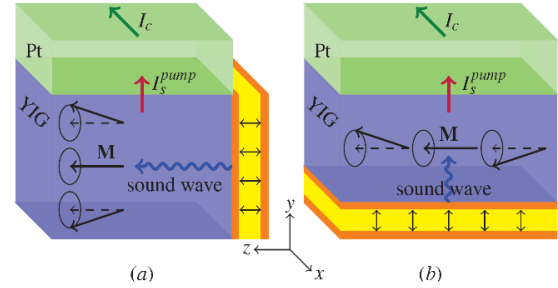


Fig. 1-1: Acoustically-induced spin pumping. Ultrasound injected by an acoustic actuator generated magnetization dynamics that pumps a spin current into an attached normal metal.
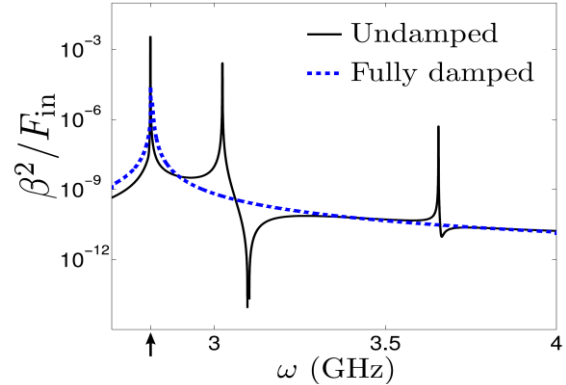


Fig. 1-2: Acoustically induced spin pumping signals as detected by the inverse spin Hall effect [4].
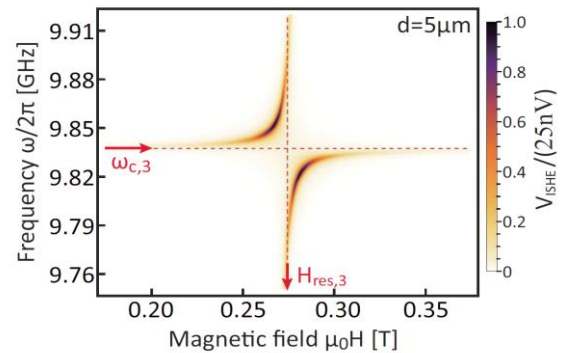


Fig. 1-3: Spin-pumping signal of the strong coupling FMR of a YIG film [5].

cavities system beyond the independent-spin and rotating wave approximations of the Tavis-Cummings model [5]. We demonstrate that strong coupling can be realized not only for the ferromagnetic resonance (FMR) mode, but also for spin wave resonances; the coupling strengths are mode dependent and decrease with increasing mode index. The strong coupling regime can be also accessed electrically by spin pumping into a heavy-metal contact.

### 3.2 Spin orbit interactions in solids

(1) Spin-orbit coupling and microscopic calculations of the anomalous and spin Hall effects: Work continued on the theory of the spin Hall effect caused by impurity scattering. Examination of the skew-scattering due to resonant scattering by $p$-orbitals was motivated by an unexplained large spin Hall effect induced by bismuth impurities in copper by the Otani group (ISSP). Previous calculations differed in both sign and magnitude from the observations. The problem of the sign, which had raised doubts in the published literature as to the origin via skew scattering was resolved. We have argued that the magnitude is due to new mechanisms of enhancement of the correlations close to the surface [6]. A related subject involved the sign of the spin Hall effect, where the discrepancy between ab initio calculations and experiments on copper alloyed with Iridium persists even with proper definitions of the transport coefficients. Here we explain the observed sign as a result of quantum fluctuations, as demonstrated by quantum Monte Carlo calculations [7]. Thus correlations, which have been argued to account for giant spin Hall effects in other alloys, here can actually change the sign of the spin Hall angle. As a test of the theory, and a means of imagining novel devices, we have investigated whether laser excitation might be used to change the 5d occupation of the Iridium orbitals and thereby reverse the spin of the Spin Hall Angle. By treating the correlations within Hartree-Fock approximations allows for fuller inclusion of all the atomic orbitals and justifies the projection onto the more limited Hilbert space needed for convergent Quantum Monte Carlo methods [8].



Fig. 1-4: A schematic figure of the change in impurity level due to the Coulomb correlation among d orbitals in a nonmagnetic impurity. The impurity level is shifted to higher in energy, decreasing the occupation number and changing the sign of the spin Hall effect.

(2) Spin dependent scattering from negatively charged Muonium: We analyzed possible explanations for the conduction electron polarization effects observed in the spin correlations of negatively charged muonium. We have discussed a new mechanism for the coherent mixing of charge states induced by hybridization with the

semiconducting host. For the resulting mixed-valence model, we have made quantitative estimates for GaAs and Si semiconductors [8].

(3) <u>STT-FMR of magnetic insulators</u>: Pure spin currents transport angular momentum without an associated charge flow. This unique property makes them attractive for spintronics applications, such as torque induced magnetization control in nanodevices that can be used for sensing, data storage, interconnects and logics. Up to now, however, most spin transfer torque studies focused on metallic ferromagnets, while magnetic insulators were largely ignored in spite of s̲uperior magnetic quality factors. We reported a theory for the current-induced STT-FMR for magnetic insulators [10] that is based on the spin Hall magnetoresistance [11], which was the main result of the REIMEI project. The Munich group took the challenge to test theory [12]. Their experiments show that in ultrathin magnetic insulators the spin torque induced magnetization dynamics can be substantially larger than those generated by the Ørsted field (see Fig. 1-5). This opens new perspectives for the efficient integration of ferromagnetic as well as antiferromagnetic insulators into electronic devices. Similar results were reported subsequently by the Argonne group [13].
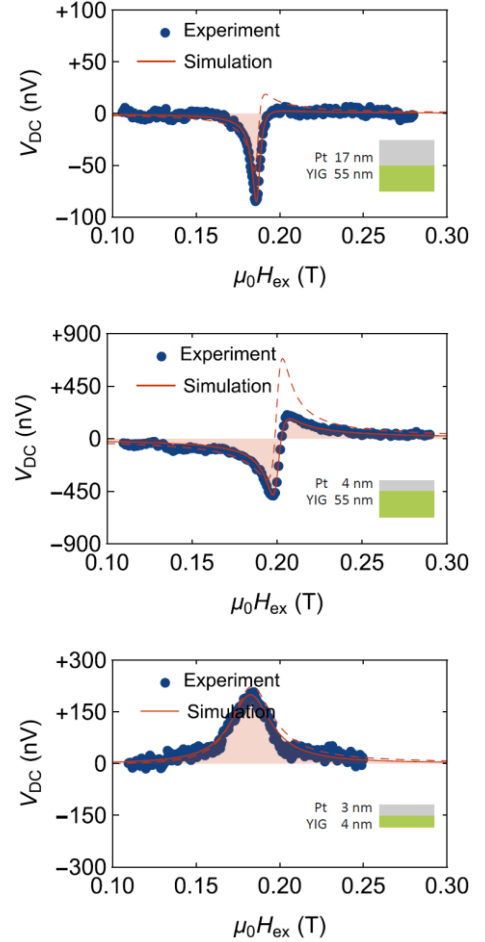


Fig. 1-5: ST-FMR in YIG|Pt [12]. The thin dashed line is for zero phase shift zero between external and internal microwaves.

## 4. Conclusion

The present Reimei project successfully addressed various aspects of the theory of spin orbit interactions in metallic normal and ferromagnetic metals, as well as heterostructures involving ferromagnetic insulators. We may conclude that we increased the grasp on important phenomena induces by the spin orbit interactions, such as the spin Hall and anomalous Hall effects in various circumstances, as well as the Muonium physics in semiconductors. By implication, we can compute the forces and torques that the electrons exert on the lattice via the same spin orbit interaction.

## Acknowledgement

## References

[1]  S. Maekawa, 'Concepts in Spin Electronics', Oxford University Press (2006).

[2]  G.E.W Bauer, A.H. MacDonald and S. Maekawa, 'Spin caloritronics', Solid State Commun. **150**, 459 (2010).

[3]  S.T.B. Gönnenwein, S. Maekawa, and G. E. W. Bauer, 'Spin mechanics', Solid State Commun. **198**, 1 (2014).

[4]  A. Kamra, H. Keshtgar, P. Yan, and G. E. W. Bauer, 'Coherent elastic excitation of spin waves, Phys. Rev. B **91**, 104409 (2015).

[5]  Y. Cao, P. Yan, H. Huebl, S. T. B. Goennenwein, and G. E. W. Bauer, 'Exchange magnon-polaritons in microwave cavities', Phys. Rev. B **91**, 094423 (2015).

[6]  Z. Xu, B. Gu, M. Mori, T. Ziman, S. Maekawa Sign change of the Spin Hall Effect due to Electron Correlation in Nonmagnetic CuIr alloys', Phys. Rev. Lett. 114, 017202 (2015).

[7]  B. Gu, Z. Xu, M. Mori, T. Ziman, and S. Maekawa. 'Enhanced spin Hall effect by electrons correlations in CuBi alloys', J. Appl. Phys. **117**, 17D503 (2015).

[8]  Z. Xu, Bo Gu, M. Mori, T. Ziman, and S. Maekawa, 'Analysis of the spin Hall effect in CuIr alloys: Combined approach of density functional theory and Hartree-Fock approximation' J. Appl. Phys. **117**,17D510 (2015).

[9]  B. Gu, T. Ziman, S. Maekawa, 'Negatively Charged Muonium as a Detector of Electron Spin Polarization: a Puzzle and a Possible Theory', JSPS, Jap. Phys. Soc. Conf. Proc. 2, 010301 (2014).

[10] T. Chiba, G. E. W. Bauer, S. Takahashi, 'Current-induced spin torque resonance for magnetic insulators', Phys. Rev. Applied **2**, 034003 (2014).

[11] Y. Chen et al., 'Theory of spin Hall magnetoresistance', Phys. Rev. B **87**, 144411 (2013).

[12] M. Schreier et al., 'Current-induced spin torque resonance of a magnetic insulator', arXiv:1412.7460.

[13] J. Sklenar et al., 'Driving and detecting ferromagnetic resonance in insulators with the spin Hall effect', arXiv:1505.07791.

# 2. Seaborgium hexacarbonyl – A new compound for superheavy element research opening the window toward organometallic chemistry of the transactinides

Ch.E. Düllmann[1,2,3], J. Even[1], A. Yakushev[2], H. Haba[4], M. Asai[5], T.K. Sato[5], H. Brand[2],
A. Di Nitto[3], R. Eichler[6,7], F. L. Fan[8], W. Hartmann[2], M. Huang[4], E. Jäger[2], D. Kaji[4],
J. Kanaya[4], Y. Kaneya[5], J. Khuyagbaatar[1], B. Kindler[2], J.V. Kratz[3], J.Krier[2],Y. Kudou[4],
N. Kurz[2], B. Lommel[2], S. Miyashita[5], K. Morimoto[4], K. Morita[4], M. Murakami[4,11], Y. Nagame[5],
H. Nitsche[9,10], K. Ooe[11], Z. Qin[8], M. Schädel[5], J. Steiner[2], T. Sumita[4], K. Tanaka[4], A. Toyoshima[5],
K. Tsukada[5], A. Türler[6,7], I. Usoltsev[6,7], Y. Wakabayashi[4], Y. Wang[8], N. Wiehl[1,3] and
S. Yamaki[4,12]

[1]Helmholtz Institute Mainz, 55099 Mainz, Germany
[2]GSI Helmholtzzentrum für Schwerionenforschung, 64291 Darmstadt, Germany
[3]Johannes Gutenberg-Universität Mainz, 55099 Mainz, Germany
[4]Nishina Center for Accelerator-Based Science, RIKEN, Wako, Saitama 351-0198, Japan
[5]Advanced Science Research Center, JAEA Tokai, Ibaraki 319-1195, Japan
[6]University of Bern, 3012 Bern, Switzerland
[7]Paul Scherrer Institute, 5232 Villigen, Switzerland
[8]Institute of Modern Physics; Chinese Academy of Sciences, 730000 Lanzhou, China
[9]University of California, Berkeley, CA 94720-1460; U.S.A.
[10]Lawrence Berkeley National Laboratory, Berkeley, CA 94720-8169 U.S.A.
[11]Niigata University, Niigata, Niigata 950-2181, Japan
[12]Saitama University, Saitama 338-8570, Japan.

Abstract

In the past, gas phase chemical studies of superheavy elements focused on volatile compounds comprising the element of interest in its highest formal oxidation state. By applying a novel combination of experimental techniques, we succeeded in the synthesis of a carbonyl compound of seaborgium – element 106, Sg – , most likely seaborgium hexacarbonyl, $Sg(CO)_6$. We have studied the volatility of this compound and its interaction with silicon oxide surfaces and compared its behavior to that of the analogous compounds of seaborgium's lighter homologs Mo and W, and to state-of-the-art quantum chemical calculations of the molecule's electronic structure and its interaction with bulk silicon oxide. Preparatory experiments have been performed to study the first bond dissociation energy of the Sg-C bond in $Sg(CO)_6$. The experimental technique used in our experiments allows producing background-free samples of $^{265}Sg$, ideal for performing nuclear spectroscopy studies of this isotope, in which an isomeric state has been identified, but is not understood theoretically.

## 1. Research objectives

Transactinide elements (TAN, atomic number Z≥104), are accessible only in nuclear fusion reactions of intense heavy-ion beams with suitable targets. Production rates of TAN range from single atoms per minute down to single atoms per week or even month, with concomitant production of orders-of-magnitude larger amounts of unwanted by-products. Some of these strongly interfere with the unambiguous detection of a single TAN atom. Harsh ionizing conditions created by the heavy-ion beam and the short half-lives of TAN nuclides severely constrain techniques that can be applied to their chemical investigations, which have reached flerovium (Fl, Z = 114) [1-3]. Chemical studies of heaviest elements are ideally suited to shed light on the influence of relativistic effects on the electron structure by the high Z [4].

Gas-phase chemical studies performed in the past five decades elucidated the chemistry of halide and oxyhalide compounds of rutherfordium (Rf, Z=104), dubnium (Db, Z=105), seaborgium (Sg, Z=106), and bohrium (Bh, Z=107), the oxyhydroxide of Sg, and the tetroxide of hassium (Hs, Z=108). In all these complexes, the metal is present in its highest formal oxidation state; i.e., all outer valence electrons participate in chemical bonding. Only copernicium (Cn, Z=112) and Fl have been studied in their elemental state. Recently, the combination of physical separation of single ions in a magnetic dipole field, combined with chemical techniques [5] was established. This technique eliminates the beam-induced plasma, which in more classical techniques prevented the formation of fragile compounds directly behind the target. Thus, this development paved the way for studies of distinct, new compound classes of the TAN. We report here the first application of this technique to a transactinide element, seaborgium along with the perspectives arising from this achievement. The work has been published in refs. [6-10] and featured in [11], and we used refs. [8-10], where the work supported by the Reimei program is described most extensively, as a basis for the account given in this report.

## 2. Research contents

### 2.1. Synthesis of volatile carbonyl complexes

For our experiments, suitable isotopes of the three homologue elements Mo, W, and Sg were produced in the nuclear fusion reactions

$^{144}$Sm($^{24}$Mg,4/5n)$^{163,164}$W ($^{163}$W: $T_{1/2}$=2.75 s, $E_\alpha$=5.38 MeV; $^{164}$W: $T_{1/2}$=6.0 s, $E_\alpha$=5.15 MeV)

$^{nat}$W($^{24}$Mg,xn)$^{201-204}$Rn ($^{201}$Rn: $T_{1/2}$=7 s / 3.8 s, $E_\alpha$= 6.7 MeV; $^{202}$Rn: $T_{1/2}$=10 s, $E_\alpha$=6.64 MeV; $^{203}$Rn: $T_{1/2}$=45s/28 s, $E_\alpha$=6.5 MeV; $^{204}$Rn: $T_{1/2}$=1.24 min, $E_\alpha$=6.4 MeV)

$^{248}$Cm($^{22}$Ne,5n)$^{265}$Sg ($^{265a}$Sg: $T_{1/2}$=8.5 s, $E_\alpha$=8.84 MeV; $^{265b}$Sg: $T_{1/2}$=14.4 s, $E_\alpha$= 8.69 MeV)
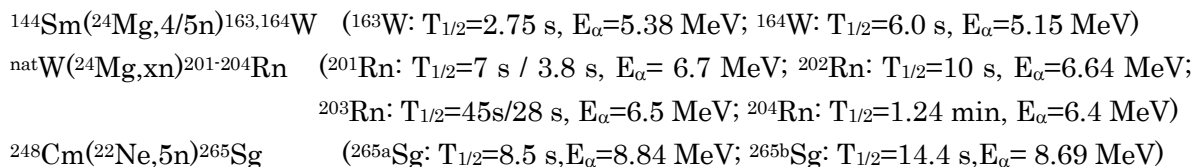
and were spatially separated from the heavy-ion beam and unwanted nuclear reaction products in the gas-filled separator GARIS at RIKEN, Wako, Japan. A schematic of the experimental setup used to study synthesis and chemical interaction of Sg(CO)$_6$ with silicon oxide surfaces is depicted in Fig. 2-1.
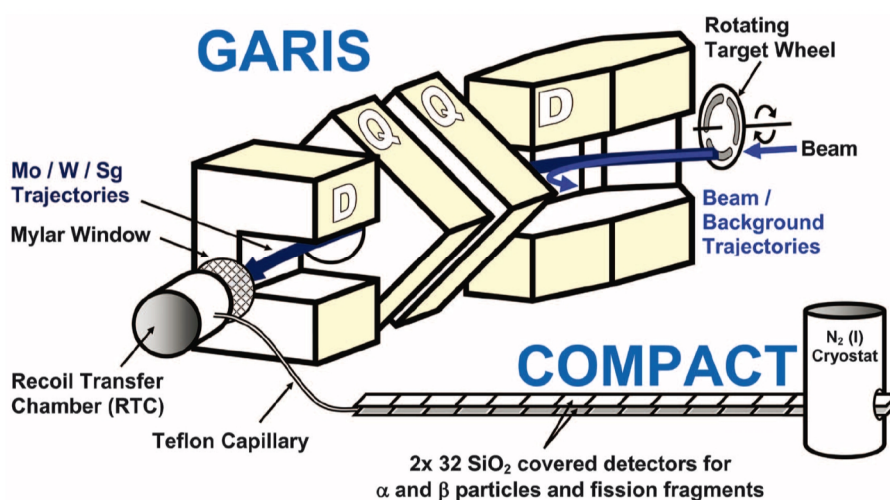
Fig. 2-1 : Schematic drawing of the experimental setup (taken from [8]).

The beam (provided by the RIKEN's RILAC accelerator) passed through the rotating target assembly. Nuclear fusion products were separated from the beam within the first dipole magnet (D in Fig. 2-1) of GARIS, focused in a doublet of quadrupole magnets (Q in Fig. 2-1) and guided by another dipole magnet to the GARIS focal plane. Mo, W, and Sg ions passed 2.5 µm, 4.4 µm, and 0.7 µm of Mylar, respectively, which reduced their kinetic energy. The ions were thermalized behind the window in a Recoil Transfer Chamber RTC [12]. The RTC was flushed with a He/CO mixture (500-750 mbar). Volatile species formed in the RTC were transported by the gas stream through a 10-m Teflon capillary to the Cryo-Online Multidetector for Physics And Chemistry of the Transactinoides COMPACT [3]. COMPACT is a gas-thermochromatography detector. The chromatography column consists of 32 pairs of Si semiconductor detectors suitable for registering time and energy resolved fission fragments, $\alpha$-, and $\beta$-particles emitted in the nuclear decay, e.g., of TAN nuclei like $^{265}$Sg and its daughter products or $^{163,164}$W and $^{87,88}$Mo, respectively. The detectors form a channel with a rectangular cross section. The surface of the detectors was covered with a 50-nm thick $SiO_2$ layer. Along the channel, a negative temperature gradient was applied using a liquid nitrogen cryostat. To calibrate the detectors, gaseous $^{219}$Rn was used, which emanated from a $^{227}$Ac source installed in the gas system.

## 2.2 Stability measurements

The rather weak bonding of the CO ligand to the central atom in the hexacarbonyl molecules of group 6 elements allows assessing an intramolecular bond, for the first time for a transactinide element. Hence, experiments focusing on measuring the first bond dissociation energy (FBDE) of the carbonyl complexes were designed. For this, a tubular flow reactor for determination of thermal stability of volatile gas phase complexes was constructed [10]. This reactor was used at a fission fragment source [13] and was also positioned between the RTC outlet and the COMPACT detector inlet. It included a room temperature Teflon tube bypass. Thus, the rate, at which the volatile complexes entered the flow reactor could be directly compared to the rate of complexes surviving the passage through the flow reactor at given

temperatures; from this, so-called decomposition curves could be obtained. The experimental setup was tested in on-line experiments with Mo and W carbonyl complexes at Bern University (Mo) and at RIKEN's GARIS separator (Mo and W). The inner surface of the flow reactor proved to sensibly affect the decomposition, suggesting a reaction driven by hot surfaces (see Fig. 2-2).
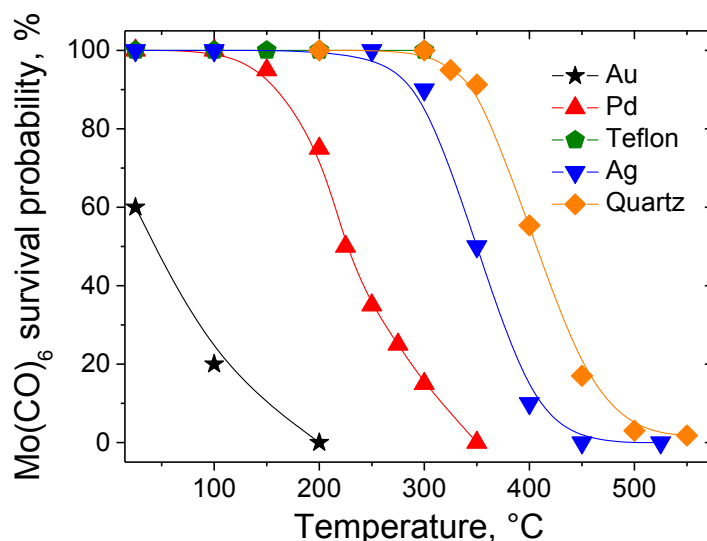


Fig. 2-2 $^{104}$Mo(CO)$_6$ decomposition curves on different surfaces, at otherwise identical experimental conditions [10].

Based on these results obtained at Bern University, silver was selected as the most promising candidate as surface material: 1) having the clear advantage of not adsorbing gaseous CO on its surface very strongly, thus providing a clean surface at elevated temperature, 2) the strong interaction of group 6 metals with noble metals such as silver allows to postulate an irreversible first-bond dissociation of the carbonyl, and 3) the non-availability of other chemical species, such as hydroxyl groups etc. like on quartz, allows to study the pure decomposition without any other chemical reaction involved.

## 3.   Research results
### 3.1. Synthesis of volatile carbonyl complexes

Two experimental campaigns at RIKEN, Wako, Japan were devoted to the synthesis and observation of Sg(CO)$_6$. To identify Sg, a search for correlated decay chains of $^{265}$Sg was performed. In the data analysis, we searched for α-particles with energies between 7.4 and 10.0 MeV, followed, within one hour, by the detection of a fission fragment or a second α-particle in the same or a neighboring detector. Thus, 15 correlated chains were found, which were assigned to the decay of $^{265}$Sg or its daughter nuclides. The likelihood that these decay chains originated from background was less than 10$^{-5}$. Additionally, three uncorrelated spontaneous fission (SF) events were registered with the COMPACT detector. As there was no fission background in the detector during the experiment and these three events were observed in the same part of the chromatography channel as the other 15 decay chains, these SF events were also assigned to

the decay of [265]Sg or its daughter nuclides. Details of the identified events are given in the supplementary material of ref. [8]. All 18 decays assigned to originate from Sg or its daughter nuclides were observed in the last third of the COMPACT detector array, as shown in the thermochromatogram depicted in Fig. 2-3, which also contains the distribution of Mo(CO)$_6$ and W(CO)$_6$.
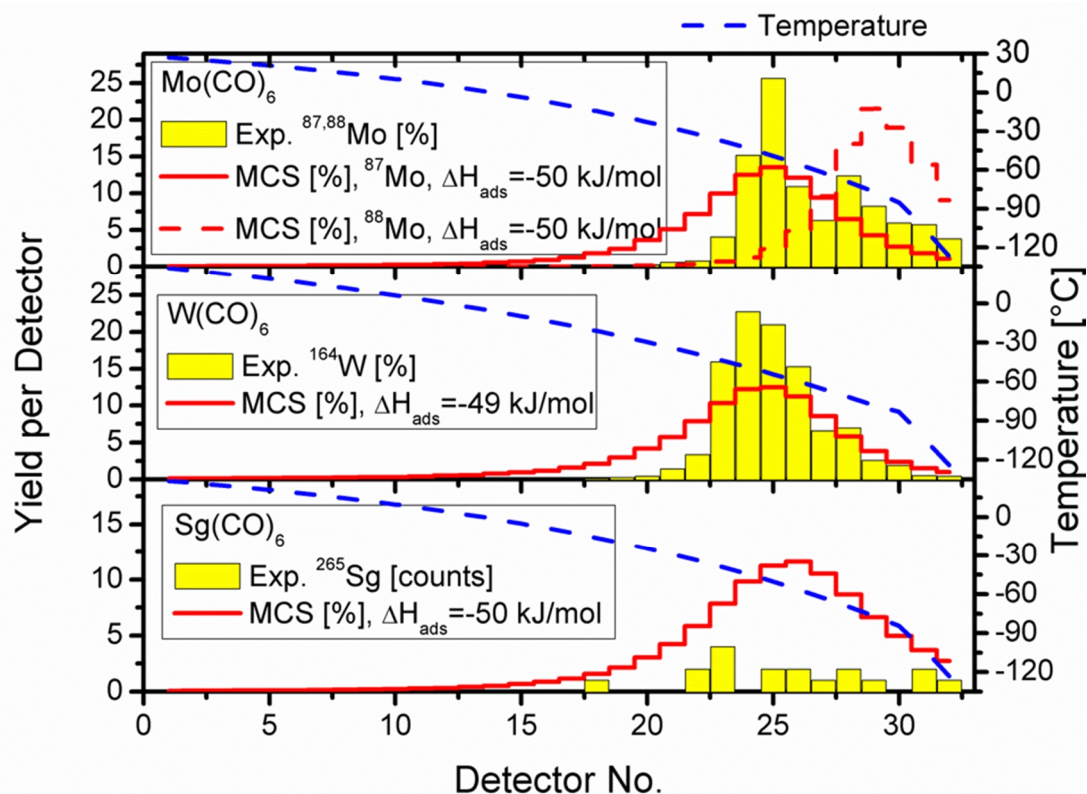


Fig. 2-3 : Deposition patterns of volatile hexacarbonyl complexes in COMPACT. The temperature gradient along the COMPACT detector array is indicated in all panels (dashed line). Top panel: experimental distribution of [87]Mo and [88]Mo (bars) and result of Monte Carlo Simulations (MCS) for [87]Mo and [88]Mo, assuming $\Delta H_{ads}$ = -50 kJ/mol (lines). Middle panel: experimental distribution of [164]W(bars) and result of MCS for [164]W(CO)$_6$ assuming $\Delta H_{ads}$ =- 49 kJ/mol (line). Bottom panel: distribution of [265]Sg and uncorrelated spontaneous fission events (bars) and results from MCS, assuming $\Delta H_{ads}$ = -50 kJ/mol (line). For details, see [8] (taken from Ref. [8]).

### 3.2 Stability measurements

Final tests of the decomposition setup were successfully performed during the second experimental campaign at RIKEN-GARIS using short-lived [87,88]Mo and [164]W. The results fully support the results obtained at Bern University using [104]Mo recoiling from a [252]Cf spontaneous fission fragment source [10]. The suggested experimental approach proved to be effective in discriminating between the stability of Mo(CO)$_6$ and W(CO)$_6$ where a 23 kJ/mol difference in their first bond dissociation energies [14] corresponded to a temperature shift of 100°C between the determined decomposition curves (see Fig. 2-4).
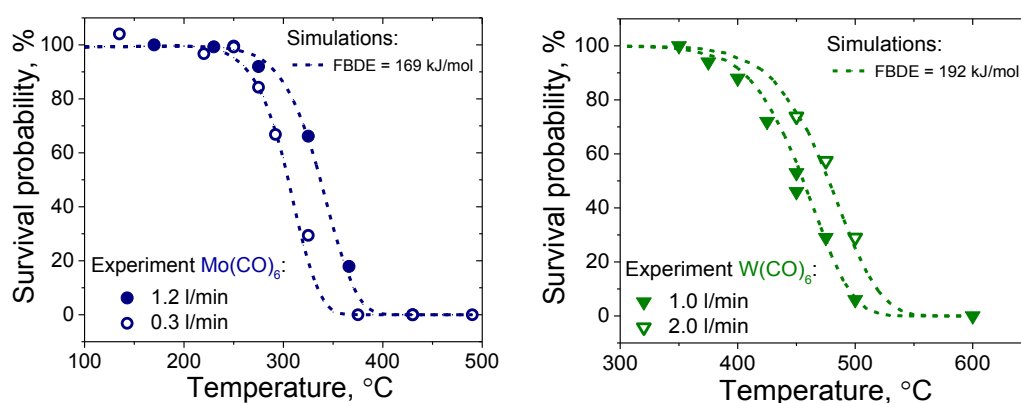
Fig. 2-4. Experimental decomposition curves of Mo (left, symbols) and W (right, symbols) carbonyl complexes at different gas flow rates together with simulated decomposition curves (lines) using for the $^{104}$Mo(CO)$_6$ decomposition (left): FBDE = 169 kJ/mol [14], and for $^{164}$W(CO)$_6$ decomposition (right): FBDE = 192 kJ/mol [14]. Statistical uncertainties are smaller than the symbols. Note the ability of the model to correctly reproduce the experimental data at different experimental conditions (e.g. gas flow rates).

As thermodynamic properties of Mo and W are known and seem to be well supported by theoretical predictions a decomposition scenario needed to be established linking the FBDE of the carbonyl complex to the measured decomposition curves.

Therefore, a Monte-Carlo based model of the decomposition of carbonyl complexes at hot surfaces was developed [10] assuming that: 1) the gas phase adsorption process follows the linear gas chromatography model as it is used for gas adsorption chromatography experiments; 2) the decomposition reaction happens only on the phase boundary in the adsorbed state and is irreversible; 3) the activation enthalpy $\Delta H^+$ of the decomposition reaction, which is determining the decomposition rate, equals to the corresponding FBDE. The results of this simulation model are shown in Fig. 2-4. The model seems to describe perfectly the experimental results obtained at various experimental conditions. This result motivated us to design an experiment to investigate the thermal decomposition of Sg(CO)$_6$ and compare it directly to the behavior of the corresponding group 6 homologs. Therefore, based on theoretical predictions [14] for the FBDE of Sg(CO)$_6$ an expectation interval for the decomposition of this complex was modelled (see Fig. 2-5) to be addressed experimentally in the near future.

## 4. Conclusion and outlook

A new compound for TAN elements has become accessible thanks to the coupling of gas phase chromatography devices such as COMPACT to physical recoil separators like GARIS. Sg(CO)$_6$ has been synthesized, and 18 decay chains assigned to $^{265}$Sg have been registered under background-free conditions (see Fig. 2-2 in [9]). Preparatory experiments with Mo and W for measuring the first Sg-C bond dissociation energy in Sg have been carried out and appear promising for extending to Sg. The superior quality of the nuclear data obtained in such experiments allows decay spectroscopy studies of $^{265}$Sg, in which an isomeric state is established [15, 16], but not currently understood theoretically (see discussion in [16]).

a

## References

[1]  A. Türler, and V. Pershina, Chem. Rev. **113**, 1237 (2013).

[2]  M. Schädel, and D. Shaughnessy, *The chemistry of superheavy elements, Ed. 2* (Springer, Heidelberg, Berlin, 2014).

[3]  A. Yakushev *et al.*, Inorg. Chem. **53**, 1624 (2014).

[4]  P. Pyykkö, and J.-P. Desclaux, Acc. Chem. Res. **12**, 276 (1979).

[5]  Ch. E. Düllmann *et al.*, Nucl. Instrum. Methods A **551**, 528 (2005).

[6]  J. Even *et al.*, Inorg. Chem. **51**, 6431 (2012).

[7]  J. Even *et al.*, Radiochim. Acta **102**, 1093 (2014).

[8]  J. Even *et al.*, Science **345**, 1491 (2014).

[9]  J. Even *et al.*, J. Radioanal. Nucl. Chem. **303**, 2457 (2015).

[10]  I. Usoltsev *et al.*, Radiochim. Acta, DOI 10.1515/ract-2015-2445 (2015).

[11]  Ch. E. Düllmann, Nature Chem. **7**, 760 (2015).

[12]  H. Haba *et al.*, J. Nucl. Radiochem. Sci. **8**, 55 (2007).

[13]  Ch. E. Düllmann *et al.*, Nucl. Instrum. Methods A **512**, 595 (2003).

[14]  C. S. Nash, and B. E. Bursten, J. Am. Chem. Soc. **121**, 10830 (1999).

[15]  H. Haba *et al.*, Phys. Rev. C **85**, 024611 (2012).

[16]  Ch. E. Düllmann, and A. Türler, Phys. Rev. C **77**, 064320 (2008).

# 3. Search for the heaviest N = Z nuclei

R. Grzywacz[1,2], A.N. Andreyev[3,4,5], G. deAngelis[6],M.A. Bentley[4], N. Brewer[2], S. Go[1] ,Z.G. Gan[7],
C.J. Gross[2], F.P. Hessberger[8], K. Hirose[3], H. Ikezoe[3], D.J. Jenkins[4], K. Kolos[1], H. Makii[3],
C. Mazzocchi[9], I. Nishinaka[3], K. Nishio[3], R. Orlandi[3], C. Petrache[10],K.P. Rykaczewski[2],
R. Leguillon[3], L.G. Sarmiento[11], J. Smallcombe[3], M. Veselsky[12], R. Wadsworth[4],
Y. Xiao[1] and Z. Zhang[7]

[1] University of Tennessee, Knoxville, USA
[2] Physics Division, Oak Ridge National Laboratory, Oak Ridge, USA
[3] Advanced Science Research Center, Japan Atomic Energy Agency, Tokai, Japan
[4] Department of Physics, University of York, Heslington, United Kingdom
[5] School of Engineering, The University of the West of Scotland, Paisley, United Kingdom
[6] Instituto Nazionale di Fisica Nucleare, Laboratori Nazionali de Legnaro, Legnaro, Italy
[7] Institute of Modern Physics, Chinese Academy of Science, Lanzhou, China
[8] GSI Helmholtzzentrum fur Schwerionenforschung, Darmstadt, Germany
[9] Faculty of Physics, University of Warsaw, Warsaw, Poland
[10] Institut de Physique Nucléaire, IN2P3-CNRS/Université Paris-Sud
[11] Lund University, Lund, Sweden
[12] Institute of Physics, Slovak Academy of Science, Bratislava, Slovakia

Abstract

Experimental program was developed at JAEA Recoil Mass Separator aiming to search for the heaviest N = Z isotopes through their alpha decays. New detector system was developed, which included particle and gamma-ray detectors. Series of experiments led to the observation of one decay sequence which could be attributed to the alpha decay chain of $^{113}$Ba.

## 1.  Research objectives

An experimental program, which aims to identify heaviest N = Z nuclei was initiated at the JAEA Tandem Laboratory. The main goal of this project is the observation of new isotopes $^{112}$Ba, $^{113}$Ba, $^{108}$Xe and $^{104}$Te produced in the fusion evaporation reactions. The selectivity required to identify the decays of these isotopes will be achieved through the observation of the characteristic complete or partial alpha decay chains: $^{112}$Ba→$^{108}$Xe→$^{104}$Te→$^{100}$Sn and $^{113}$Ba→$^{109}$Xe→$^{105}$Te→$^{101}$Sn. A decay fingerprint is provided by the pulse shape of the detector signal due to the fast decay of the alpha emitting tellurium member of the chain. The $^{112}$Ba is the heaviest N = Z nucleus which can be synthesized in fusion reaction of stable beam and target combination. The observation of its alpha emission and measurement of the decay energy alone will contribute to the modeling of the nuclear properties near the proton drip line. Specifically, unique type of enhancement of the alpha particle emission from nuclei in the vicinity of $^{100}$Sn was proposed [1] and was attributed to increased alpha particle pre-formation in nuclei where valence protons and neutron occupy identical shell model orbitals. This phenomenon is also linked to nuclear proton-neutron pairing which can be uniquely studied in

N = Z systems [2]. The degree of pre-formation can be deduced from observation of the alpha decay lifetime ($T_{1/2}$) and decay energy ($Q_\alpha$). The determination of decay $Q_\alpha$ values will be used to verify theoretical mass predictions in the $^{100}$Sn region and, in particular, it will also reflect the role of proton-neutron correlations in the region of the heaviest N = Z nuclei.
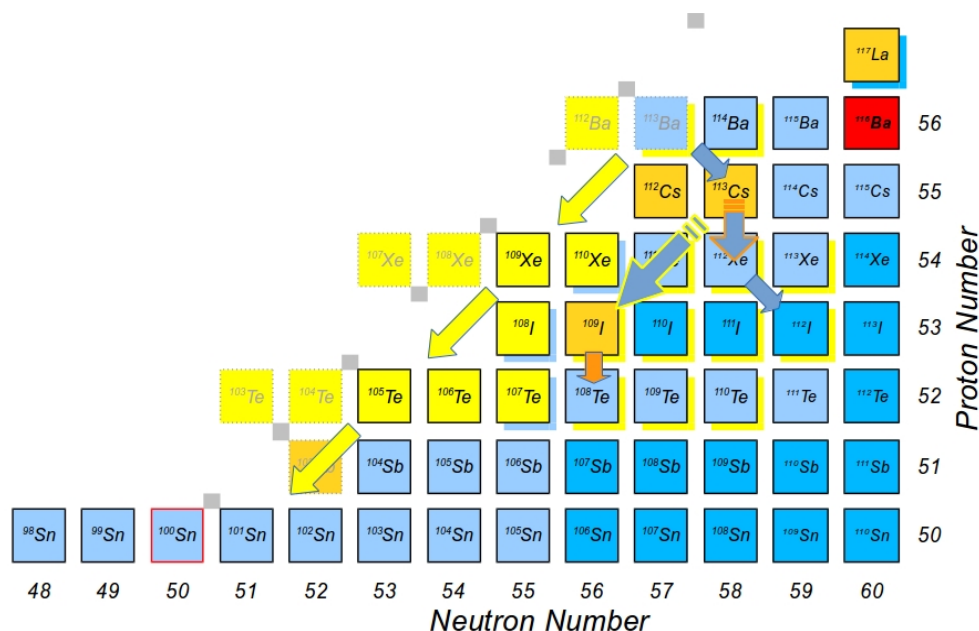


Fig. 3-1 The region of the chart of nuclei with color codes indicating prevalent decay modes: blue - beta decay, orange – proton emission, yellow-alpha decay. Red square indicates compound nucleus $^{116}$Ba for the $^{58}$Ni+$^{58}$Ni reaction. The arrows indicate possible decay channels of $^{113}$Ba.

## 2.   Research contents

Proof of principle experiments were conducted, which demonstrated the capability of JAEA Tandem and RMS [3] to perform these challenging experiments. First experiments used $^{58}$Ni beam at 225 MeV beam and 0.5 mg/cm$^2$-thick $^{54}$Fe to synthesize the alpha emitters in the $^{100}$Sn, see Fig. 3-1. This and subsequent experiments used 65 μm thick double sided silicon strip detector (DSSD)
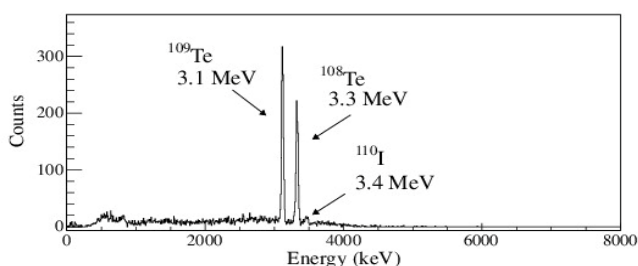


Fig. 3-2 The energy spectrum of the DSSD signals recorded at the focal plane of the JAEA RMS using reaction of $^{58}$Ni+$^{54}$Fe.

equipped with digital data acquisition system [4]. The conventional ion-decay correlation method was used. In a follow up experiment, we measured the $^{109}$Xe→$^{105}$Te→$^{101}$Sn decay chain by exploiting the characteristic pulse shape signature as was previously demonstrated in [5,6] in order to prove that these very demanding  measurements can be performed at the JAEA

facility, four pileup events with characteristics similar to the one shown in Fig. 3-3 were detected within about 3 shifts of the measurement. Finally in December of 2014 we performed an experiment searching for the decay of $^{113}$Ba using $^{58}$Ni beam and $^{58}$Ni target combination with 245 MeV and 250 MeV beam energies. Several new improvements were made to enable this experiment, see Fig. 3-3. First, the JAEA rotating target was implemented, with large area, thin target foils produced at GSI and mounted to the target wheel. Second, new complex vacuum chamber was constructed at JAEA, which enabled more flexibility to host detector systems. Third, a new liquid cooled detector mount was developed at ORNL, which was housed inside a thin aluminum chamber enabling the detection of gamma rays with minimal attenuation of the photons. The detection system was surrounded by the high efficiency NaI array, which was used as a very efficient gamma ray detector. The experiment relied on detecting the characteristic decay pattern of the $^{109}$Xe→$^{105}$Te→$^{101}$Sn which has to occur with few tens of milliseconds after the $^{113}$Ba alpha decay in the same DSSD pixel. The gamma ray detector serves a double purpose, suppressing the background associated with beta decays of implanted activities and, in addition, providing additional tagging for the gamma rays associated with alpha decay to excited states in the daughter nuclei [6].

## 3.　Research results

During the $^{113}$Ba experiment we have observed on-line one clean pileup event, which belongs most likely to the decay of $^{109}$Xe and is originating from alpha decay of $^{113}$Ba, however due to the shallow implantation of the $^{113}$Ba recoils in the DSSD, in this case the alpha particle from original $^{113}$Ba decay escaped without being detected. Assuming, that the detection probability for the full energy alpha particle is about 50%, the detection probability of this particular event is (50%)$^3$ =12.5%. We are presently investigating the correlations between alpha decays using gamma ray
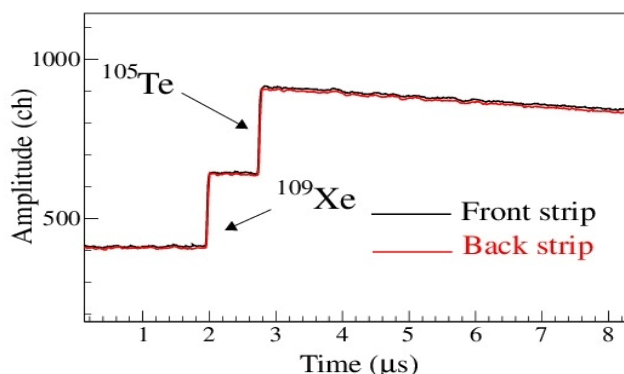


Fig 3-3　Pile-up trace from the $^{109}$Xe→$^{105}$Te→$^{101}$Sn decay chain observed at ASRC RMS focal plane using digital signal processing technique and detection method used in ref. [Lid06,Dar10]

detector as additional tagging tool, which would enable clear identification of the $^{109}$Xe decay chain which has high probability to be associated with the gamma ray, see Ref. [6]. The measured rate of $^{113}$Ba alpha decays of less than one per day, and is much smaller than expected (one per hour) based on the cross section calculations using HIVAP code [7]. A possible explanation of this fact is the higher than predicted relative beta decay branching ratio which would be smaller than 1% instead of expected 10% [8]. The data analysis is in progress and two main strategies are implemented: one is to find the other missing alpha decays by looking for evidence for partial decay chains, and other to look for the beta decay events through

observation of proton emission events from the very short-lived ground state of $^{113}$Cs ($T_{1/2}$=18 μs), which is beta decay daughter of $^{113}$Ba.
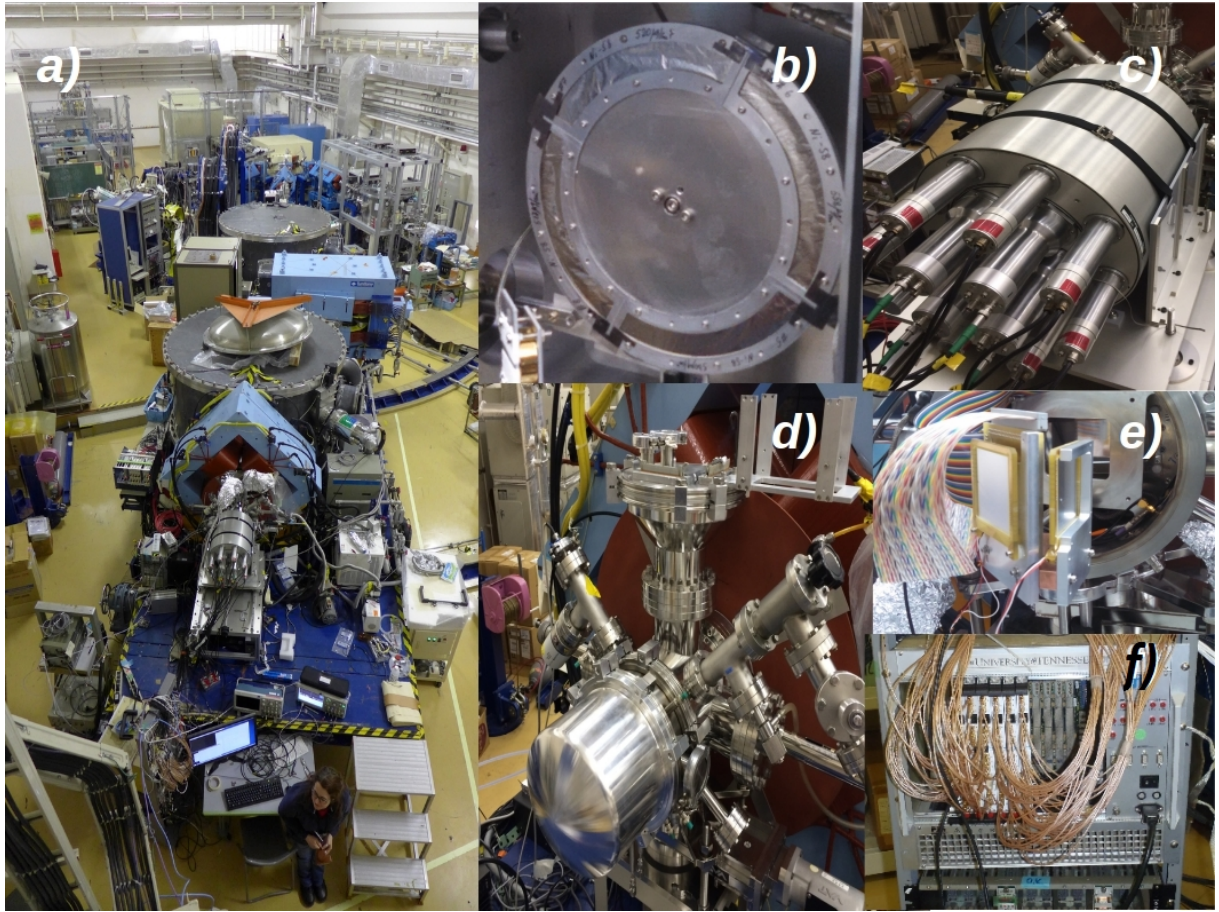


Fig. 3-4 The experimental setup used in presented research the JAEA RMS [3] a) The key components are shown: rotating target b), high efficiency NaI segmented detector c), vacuum chamber d) containing the detector system e), and digital electronics f).

## 4. Conclusion

In the series of experiments, the feasibility of the JAEA RMS to be able to perform some of the most difficult alpha decay experiments in the $^{100}$Sn region was proven. We have tentatively identified one event of $^{113}$Ba during two weeks long experiment. From the present state of the data analysis we conclude, that the alpha decay branching ratio of $^{113}$Ba is likely to be in 1% range instead of 10% predicted previously. This low branching ratio value is more consistent with recent JAEA [9] evaluation.

References

[1] R. Macfarlane and A. Siivola, Phys. Rev. Lett. **14**, 114 (1965).

[2] B. Cederwall et al. Nature **469**,   68 (2011).

[3] H. Ikezoe et al. Nucl. Instr. Meth. B **126**, 340(1997).

[4] R. Grzywacz et al.,NIM B **261**, 1103 (2007).

[5] S. N. Liddick et al., Phys. Rev. Lett. **97**, 082501 (2006).

[6] I. Darby et al., Phys. Rev. Lett. **105**, 162502 (2010).

[7] W. Reisdorf et al. Nucle Phys. A**438**, 212 (1985).

[8] C. Xu and Z.Ren, Phys. Rev. C **74**, 037302 (2006).

[9] H. Koura, J. Nucl. Sci. Technol. **49**, 816 - 823 (2012).

# 4. Initial processes of radiation effects on genomic stability

Marie-Anne Hervé du Penhoat[1], Evelyne Sage[2], Chantal Houée-Lévin[3], Sandrine Lacombe[4], Marie-Françoise Politis[5], Alain Touati[1], Rodolphe Vuilleumier[6], Marie-Pierre Gaigeot[5], Riccardo Spezia[5], Frank Wien[7], Kentaro Fujii[8], Yudai Izumi[8], Naoya Shikazono[9] and Akinari Yokoya[8]

[1] Institut de Minéralogie, de Physique des Matériaux et de Cosmochimie, Sorbonne Universités - UPMC Univ Paris 06, UMR CNRS 7590, MNHN, IRD UMR 206, France
[2] Laboratoire de Biologie des Radiations, Institut Curie, France
[3] Laboratoire de Chimie Physique, UMR 8000, Université Paris Sud, France
[4] Institut des Sciences Moléculaires d'Orsay, UMR 8214, Université Paris Sud, France
[5] Laboratoire Analyse et Modélisation pour la Biologie et l'Environnement, UMR 8587, Université d'Evry val d'Essonne, France
[6] Département de Chimie, École Normale Supérieure, Paris, France
[7] SOLEIL Synchrotron, France
[8] Advance Science Research Center, Japan Atomic Energy Agency, Japan
[9] Quantum Beam Science Center, Japan Atomic Energy Agency, Japan

Abstract

We report the progresses and current status of the REIMEI study on "Initial processes of radiation effects on genomic stability", which has been implemented under the international collaboration between France and Japan. The project has three sub-projects; 1) Theoretical study of DNA strand scission and its experimental verification; 2) biomolecular modifications explored by synchrotron spectroscopic techniques; 3) DNA damage repair in eukaryote and prokaryote cells. These sub-projects are closely associated with each other. For the first one, a theoretical study on the fragmentation pattern of doubly ionized deoxyribose (dR) has been performed at the femtosecond timescale for both isolated and hydrated deoxyribose molecules. The results showed that the early processes after the ionization strongly depend on the water hydration. Particularly, ultrafast proton transfers from the ionized dR molecule towards hydration water molecules could prevent some of the dissociation pathways measured in isolated dR. This was well consistent with the experimental results of photodesorbed ions from dry or hydrated deoxyribose films exposed to monochromatic soft X-rays, that were studied using a SPring-8 beamline. As for the second sub-project, synchrotron radiation circular dichroisim (SR-CD) measurements for histone proteins extracted from human cells were performed in the UV and far-UV regions to explore the origin of signal transduction of DNA repair processes. Compared to unirradiated cells, a relative increase in α-helix structure and decrease in other secondary structures was observed in X-irradiated cells. These structural alterations persisted for at least 24 hours, which is substantially longer than the 2 hours generally known to be required for DNA double strand break repair. Further study to extend to a far-UV region is also being performed to obtain free energy changes linked to conformational

modifications in Histone. Finally, for the third sub-project, preliminary experiments using E. coli cells have also been performed focusing on the role of DNA polymerases on the mutagenic potential of clustered DNA lesions.

## 1. Research objectives

It is well known that genomic stability of living organisms is seriously affected by ionizing radiations. The understanding of radiation effects has been recognized as one of the major subjects to provide noxious aspects and possible helps for low-dose effects of diagnostic radiation, or of radon absorption in buildings, or of nuclear accidents such as the recent one in Fukushima. Moreover such studies can also reveal new aspects of evolution of life in terms of adaptation to radiation-stresses from the environment during geological ages.

The main purpose of our REIMEI project is to clarify the physicochemical processes of radiation effects on biomolecules and the biological responses to radiation damage in cells. The project consists of three research lines (sub-projects), which have a common objective: to explore radiation effects on living cells and bio-molecular damage using spectroscopic and biochemical approaches.

## 2. Research contents

### 2.1 Sub-project 1: Theoretical study of DNA strand scission and its experimental verification

We have addressed the first sub-subject, how the deoxyribose (dR) molecule dissociates after the removal of an electron from an oxygen K-shell. Core ionization of DNA atoms were indeed shown to induce irreparable double strand breaks in cells [1]. Because the sugar moiety is a major component of the DNA chain, we expect to obtain one of the mechanisms of DNA-strand-breakage, which may be a part of the clustered DNA damage (see Sub-project 3) induced in cellular genomes exposed to ionizing radiation (Fig 4-1).
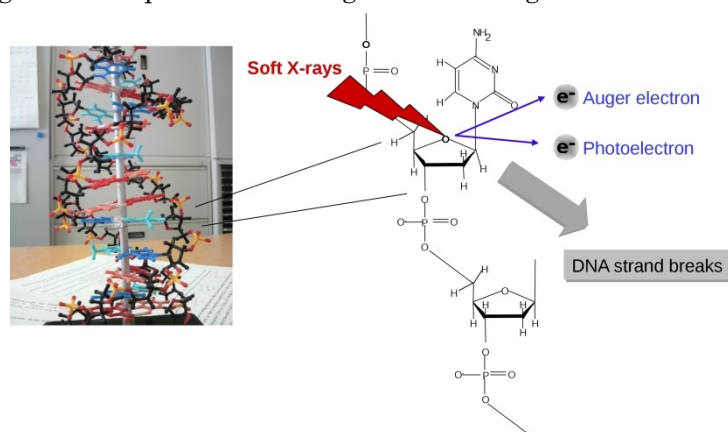


Fig. 4-1 The removal of core electrons by soft X-rays leads to the emission of an Auger electron in addition to the photoelectron. These electrons can, in turn, locally damage DNA.

In order to study radiation damage to deoxyribose molecules, we applied the theoretical approaches we have developed to investigate the fragmentation pattern of core [2] and doubly ionized molecules [3] in the condensed phase. To that aim, we use state-of-the-art ab initio

Density Functional Theory (DFT) based Molecular Dynamics simulations. The ultrafast dissociation dynamics of the core ionized biomolecule, prior to Auger decay, is first modeled for about 10 fs to generate initial configurations (atomic positions and velocities) for the subsequent dynamics of the doubly ionized biomolecule after Auger decay. In the gas phase, we have investigated three dR conformations [4]: The furanose form corresponds to that of this sugar in DNA, whereas the pyranose form is predominant in the gas phase and may thus be compared to experiments [5]. In order to probe the role of hydration, we have compared the ultrafast dissociation dynamics of core ionized deoxyribofuranose either isolated or embedded in liquid water [6].

We also prepared a sample manipulating system for water vapor exposure (Fig. 4-2) which was installed in the Japanese synchrotron, SPring-8. Using this system, we performed experiments to examine the fragmentation pattern of hydrated deoxyribose molecule with two holes (following core ionization and Auger effect) after soft X-irradiation to verify the theoretical prediction.
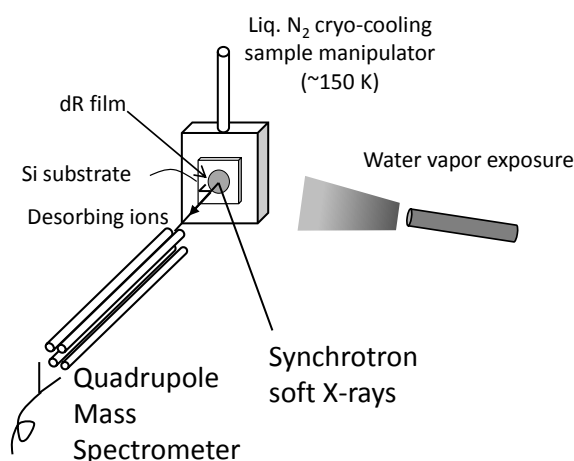


Fig. 4-2 Experimental setup of a quadrupole mass spectrometer in SPring-8 using a hydrated deoxyribose film.

2.2 Sub-project 2: Biomolecular modifications explored by synchrotron spectroscopic techniques

DNA repair processes involve dramatic alterations of chromatin structures, such as chromatin remodeling in order to make DNA repair proteins more accessible to damaged DNA sites [11]. It is thought that chromatin structure remodeling basically occurs by post-translational modifications of histone proteins, around which DNA wraps in eukaryotic nuclei [9]. However, direct evidences are still very scarce. In this research project, we have focused on the secondary structural alterations of histone H2A-H2B mediated by the DNA damage responses, and tried to use circular dichroism (CD) spectroscopy to observe the conformational change in a chromatin architecture, particularly histone proteins, induced by ionizing irradiation. Using a synchrotron radiation (SR) facility (SOLEIL, France), we measured the SR-CD spectra of histone H2A-H2B, of which wide spread modifications are known to occur during DNA damage repair processes [12]. The histones were extracted from

non-irradiated or X-irradiated human cells in an attempt to reveal structural alterations of histone proteins during DNA damage responses.

### 2.3 Sub-project 3: Molecular biology study of processing of cluster DNA damage

This project has focused on the repair and the mutagenic potential of a subset of radiation-type DNA damage. Similarities/difference of DNA damage repair strategy between distinct microstructures of clustered DNA damage were highlighted to reveal the mechanisms of genome stability maintenance. DNA with model synthetic DNA damage was subjected for analysis of their mutagenicity. Clustered damage site-carrying duplexes were introduced into *Escherichia coli* (Fig. 4-3). The project will help to understand how such complex damage is repaired.
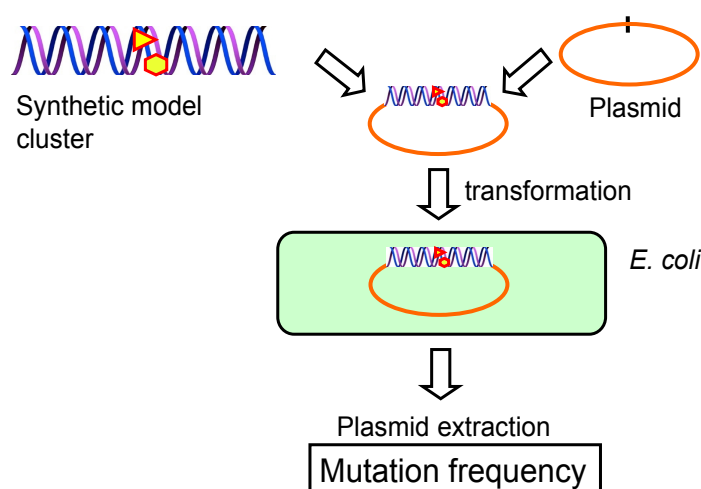


Fig. 4-3. Outline of the experiment. A model cluster ligated into a plasmid was transfected into bacteria, E. coli. Amplified plasmids were extracted to measure the mutation frequency as a result of the cluster.

## 3. Research results

### 3.1 Sub-project 1: Theoretical study of DNA strand scission and its experimental verification

In the gas phase, we have focused on the dissociation dynamics of ground state $dR^{2+}$, after either 5 or 10 fs of core-hole dynamics [4]. We show that the fragmentation process is relatively independent of the oxygen atom struck or of the duration of the core vacancy. It however depends on the sugars conformation (furanose or pyranose). Preliminary results on the dissociation of $dR^{2+}$, removing the two electrons from deeper molecular orbitals (MO), show that the dissociation process may strongly depend on the localization of the MO within the molecule. Full electron quantum calculations of most probable channels of Auger deexcitation are thus important. When embedded in liquid water, we show that the core-ionization of an oxygen atom within 2-deoxy-D-ribose may induce ultrafast proton transfers towards nearby water molecules, before Auger decay [6]. We have also modelled the dissociation dynamics of the doubly ionized sugar, removing the two electrons from deep molecular orbitals located on each of the four oxygen atoms. Preliminary results show selective bond scission.

We measured mass spectrum of ions desorbing from hydrated dR films exposed to monochromatic soft X-rays (560 eV). The X-ray photons ionize K-shell electrons of oxygen atoms in DNA. Hydrated dR samples were prepared in vacuum by water vapor exposure to the cooled (~150 K) dR film deposited on a Si substrate. Experiments using synchrotron soft X-rays were performed at a synchrotron beamline in SPring-8, Japan. We observed desorbing ions such as $H^+$, $CH_x^+$, $C_2H_x^+$, $CH_xO^+$, $C_3H_x^+$, and $C_2H_xO^+$ (x=1, 2, 3, or 4) by a quadrupole mass spectrometer (Fig. 4-4(a)). These ions are produced by C-C or C-O bond scission in the dR molecule. Except for $H^+$, the yields of those ions decreased when one layer of water molecules was deposited onto the film (Fig. 4-4(b)). This result suggests that the water molecules act as a quencher suppressing a Coulomb explosion, and thus play a protective role in a cell nucleus to prevent DNA strands from breaking.
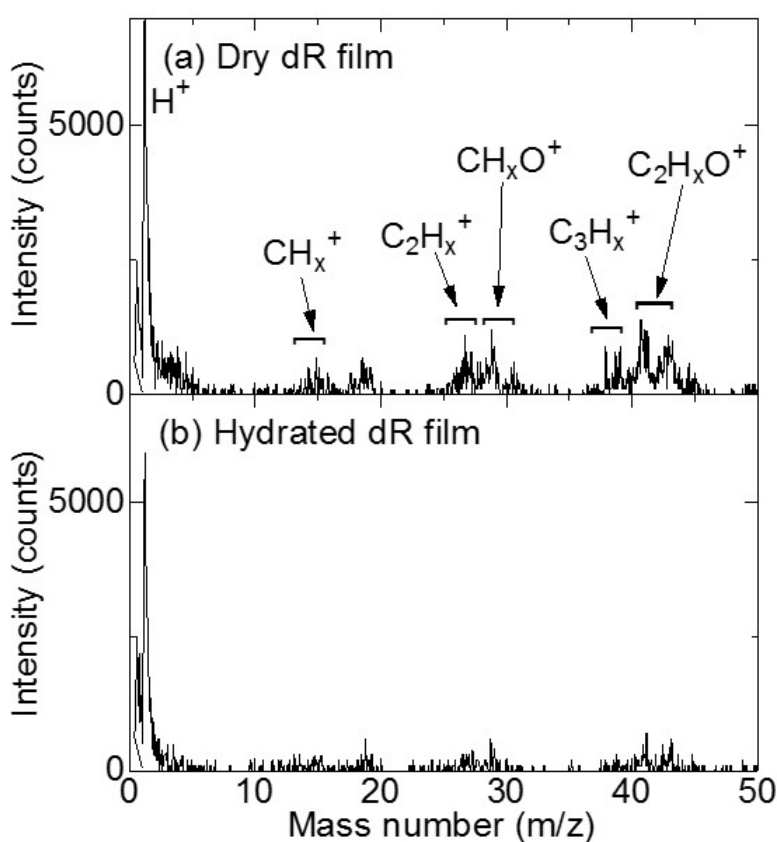


Fig. 4-4 Desorbing ion mass spectra of (a) dry dR film and that of (b) hydrated dR film obtained during 560 eV soft X-ray exposure.

### 3.2 Sub-project 2: Biomolecular modifications explored by synchrotron spectroscopic techniques

Histone H2A-H2B was extracted from unirradiated or 40-Gy-irradiated human cancer, HeLa-S. FUCCI, cells and dissolved in 10 mM Tris-HCl buffer (pH = 8.0) supplemented with 90 mM sodium fluoride. Prior to the SR-CD beamtime, we verified that the CD signal from the prepared protein sample could surely be detected using a conventional CD spectrometer in UV region (195-260 nm) [14]. Then, the SR-CD spectroscopy was carried out at DISCO beamline of SOLEIL, France (Wien et al., 2013) in a far-UV region (175 to 260 nm). The spectra were then

analyzed by using BeStSel program [10], applied at a wavelength region of 180 to 250 nm, to extract the percentages of helixes and sheets structure of the samples.

Fig. 4-5 shows SR-CD spectra of H2A-H2B extracted from unirradiated and irradiated cells measured at 298 K [15]. Both samples showed a positive peak at around 190 nm and two negative peaks at around 208, and 222 nm. Those peaks are characteristic of α-helix structure. The analysis revealed that the α-helix content of unirradiated and that of irradiated samples are 18 and 29%, respectively, at 298 K. This increment, induced by X-irradiation to cells altered the structure of H2A-H2B, and persists for at least 24 hours in X-irradiated cells [14]. In order to examine the direct radiation damage to histone, we exposed a solution of histone extracted from the cells to X-rays, and measured the CD spectrum. Contrary to the results of exposures to cells, the content of α-helix decreased by the irradiation, indicating that radiation damage to the protein causes different structural changes from that induced in the irradiated cells. From these results, the increase of the α-helix in histone extracted from the exposed cells is inferred to be caused by some chemical modifications such as phosphoryration or acetylation, and not to be caused by direct radiation damage to the protein. The modifications of the secondary structure of H2A-H2B is thought to be a result of cellular response to radiation, which might be important to trigger the DNA repair responses.
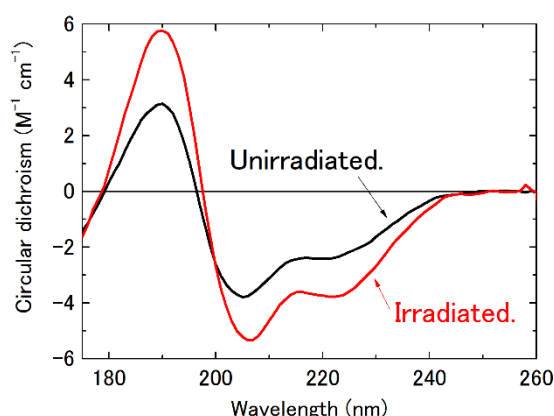


Fig. 4-5 VUV SR-CD spectra of H2A-H2B extracted from unirradiated (black) and irradiated (red) HeLa cells. The measurements were performed at 298 K.

### 3.3　Sub-project 3:　Molecular biological study of processing of cluster DNA damage

We firstly examined the role of Pol I in mutagenesis of bi-stranded clustered damage sites, consisting of a combination of DNA lesions, such as a strand break, an apurinic/apyrimidinic (AP) site, and an 8-oxo-7,8-dihydroguanine (8-oxoG) [7]. Pol I is responsible for repair synthesis during base excision repair and for gap filling during lagging strand synthesis during replication. Mutation frequencies were higher in Pol I-deficient than in Pol I-proficient cells, indicating that Pol I plays an important role in minimizing mutations induced as a result of clustered lesions. We further investigated the outcome of clusters composed of a rapidly excised uracil (u) and two damaged bases, 5-hydroxyuracil (hU) and 8-oxog, which are excised more slowly [8]. We demonstrated that mutagenesis at hU is correlated with excision of the U placed on the opposite strand. Excision of U likely initiates the loss of U-8-oxoG -carrying strand,

resulting in enhanced mutagenesis at hU present on the opposite strand. Our results highlight the importance of the kinetics of excision by base excision repair enzymes as well as the extent of repair of the strand breaks, and provide evidence for the mutagenic role of replication fork collapse during the processing of complex damage. The roles of various polymerases in the precessing of clustered DNA damage arising in mammalian cells will be our next target.

## 4. Conclusion

The REIMEI project has been implemented since July 2012 for two years. Using the REIMEI budget, interexchange of scientists between France and Japan has been performed to discuss the detail of the project. We organized workshops of "Initial Processes of Radiation Effects on Genomic Stability" from March 21st to 22nd in 2013 at UPMC in Paris, and March 12th to 13th in 2014 at JAEA in Tokai to report and discuss current statuses of each sub-projects. Some noteworthy progresses have been already published or submitted to journals. We keep going for further exchange of researchers, particularly young scientists including graduated students, between France and Japan to accelerate research activities as well as to ensure international competitiveness in the new areas of research.

## Acknowlegments

## References

[1] Hervé du Penhoat, M.A., Eschenbrenner, A., Abel, F., Boissière, A., Guigner, J.M., Chetioui, A., Politis, M.F., Touati, A., Sage, E., Jenner, T.J., Stevens, D.L. and Hill, M.A., Double strand-break induction and repair in V79-4 hamster cells: The role of core ionisations, as probed by ultrasoft Xrays. *Int. J. Radiat. Biol.* **86**, 205-219 (2010).

[2] Stia, C.R., Gaigeot, M.P., Vuilleumier, R., Fojón, O., Hervé du Penhoat, M.A. and Politis, M.F., Theoretical investigation of the ultrafast dissociation of core-ionized water and uracil molecules immersed in liquid water. *Eur. Phys. J. D* **60**, 77-83 (2010).

[3] López-Tarifa, P., Gaigeot, M.P., Vuilleumier, R., Tavernelli, I., Alcamí, M., Martín, F., Hervé du Penhoat, M.A. and Politis, M.F., Ultrafast Damage Following Radiation-Induced Oxidation of Uracil in Aqueous Solution. *Ang. Chem.* **52**, 3160 (2013).

[4] Hervé du Penhoat, M.A., Ghose, K., Gaigeot, M.P., Vuilleumier, R., Fujii, K., Yokoya, A. and Politis, M.F., Investigation of the fragmentation of core-ionised deoxyribose: A study as a function of the tautomeric form. *Phys. Chem. Chem. Phys.* **17**, 48, 32375-32383 (2015).

[5] Ha, D., Huels, M., Huttula, M., Urpelainen, S. and Kukk, E., Experimental and ab initio study of the photofragmentation of DNA and RNA sugars. *Phys. Rev. A* **84**, 033419-033429 (2011).

[6] Fujii, K., Izumi, Y., Narita, A., Ghose, K., López-Tarifa, P., Touati, A., Spezia, R., Vuilleumier, R., Gaigeot, M.P,, Politis, M.F., Hervé du Penhoat, M.A. and Yokoya, A., (private communication).

[7] Shikazono, N., Akamatsu, K., Takahashi, M., Noguchi, M., Urushibara, A., O'Neill, P. and Yokoya, A., Significance of DNA polymerase I in in vivo processing of clustered DNA damage. *Mutat Res.* **749**, 9-15 (2013).

[8] Sedletska, Y., Radicella, J.P. and Sage, E., Replication fork collapse is a major cause of the high mutation frequency at three-base lesion clusters. *Nucleic Acids Res.* **41**, 9339-9348 (2013).

[9] Hunt, C.R., Ramnarain, D., Horikoshi, N., Iyengar, P., Pandita, R.K., Shay, J.W., et al., Histone modifications and DNA double-strand break repair after exposure to ionizing radiations. Rad Res 2013; 179:383-92.Micsonai, A. et al. (2013).

[10] Micsonai, A., Wien, F., Kernya, L., Lee, Y. -H., Goto, Y., Réfrégiers, M., and Kardos, J., Accurate secondary structure prediction and fold recognition for circular dichroism spectroscopy, *Proc. Natl. Acad. Sci. USA*, **112**, E3095-E3103 (2015).

[11] Polo, S.E., Reshaping chromatin after DNA damage: The choreography of histone proteins. *J Mol. Biol.* **427**, 626-36 (2015).

[12] Rogakou, E.P., Pilch, D.R., Orr, A.H., Ivanova, V.S. and Bonner, W.M., DNA double-stranded breaks induce histone H2AX phosphorylation on serine 139. *J. Biol .Chem.* **273**, 5858-68 (1998).

[13] Wien, F., Miles, A.J. and Lees, J.G., Vrønning Hoffmann S, Wallace BA, VUV irradiation effects on proteins in high-flux synchrotron radiation circular dichroism spectroscopy. *J. Synchrotron Rad.* **12**, 517-23 (2005).

[14] Izumi, Y., Yamamoto, S., Fujii, K. and Yokoya, A. Secondary structure alterations of histones H2A and H2B in X-irradiated human cancer cells: Altered histones persist in cells for at least 24 hours. *Radiat. Res.* **184**, 5, 554-558 (2015).

[15] Izumi et al (SOLEIL experiment), private communication.

(Contact)

Marie-Anne Hervé du Penhoat

Institut de Minéralogie, de Physique des Matériaux et de Cosmochimie

Université Pierre et Marie Curie

4 place Jussieu, 75005 Paris, FRANCE

E-mail: Marie-Anne.Penhoat@impmc.jussieu.fr

# 5. Muon spin relaxation studies of itinerant-electron magnets without constituent magnetic elements: Sc₃In and TiAu

Lian Liu[1], Benjamin Frandsen[1], Sky Cheung[1], Yasutomo J. Uemura[1], Eteri Svanidze[2],

Jiakui K. Wang[2], Emilia Morosan[2], Jeff W. Lynn[3], T. Medina[4], Timothy J. S. Munsie[4],

Graeme M. Luke[4], Deng Zheng[5] and Changqing Jin[5]

[1]Department of Physics, Columbia University, New York, NY 10027, USA

[2]Department of Physics and Astronomy, Rice University, Houston, TX 77005, USA

[3]NIST Center for Neutron Research, National Institute of Standards and Technology, Gaithersburg, MD 20899, USA

[4]Department of Physics and Astronomy, McMaster University, Hamilton, Ontario L8S 4M1, Canada

[5]Institute of Physics, Chinese Academy of Sciences, Beijing 100190, China

Abstract

Supported partly by the JAEA REIMEI project, MuSR studies have been performed at TRIUMF, Vancouver to demonstrate static magnetic order in novel itinerant magnets $(Sc,Lu)_3In$ and TiAu. In both systems composed of constituent atoms without having unpaired d- or f-electrons, static magnetic order was detected with phase separation and without dynamic critical phenomena. This behavior is similar to the case of another itinerant magnet MnSi in applied pressure. Together with the neutron scattering results which detected antiferromagnetic Bragg peak, TiAu has been established as the first known example of antiferromagnet based on weak magnetism of itinerant electrons.

## 1. Research Objective

Despite the success of the Stoner model [1] and the subsequent improvements by the self-consistent renormalization (SCR) theory in which spin fluctuations were accounted for [2], the nature of weak itinerant magnetism remains elusive. One generic feature of the weak magnetic order of itinerant-electron systems is the possibility of a first-order phase transition [3]. While many experimental techniques [4] have been used to investigate this phenomenon, we have focused on the muon spin relaxation (μSR) technique. The absence of dynamic critical fluctuations was observed in the itinerant helimagnet MnSi near the pressure-tuned quantum evolution to the paramagnetic phase [5]. Similarly such tendencies were seen in the itinerant ferromagnet $(Sr,Ca)RuO_3$ tuned with (Sa,Ca) substitutions close to the disappearance of static magnetic order around a Ca concentration of 0.7 [5].

For studies of weak magnetism due to itinerant electrons, systems without constituent atoms having unpaired spins (such as Fe, Ni or Mn) can provide unique and valuable insights, since there will be no contribution from "localized spins" associated to constituent atoms and all the magnetism should be clearly due to the effect of band structure. Of magnetic metals without magnetic constituents, only two itinerant ferromagnets (IFMs), $Sc_3In$ [6] and $ZrZn_2$ [7], have

been known for fifty years. We synthesized pure and Lu-substituted $(Sc,Lu)_{3.1}In$ to perform systematic studies of the quantum phase transition (QPT). TiAu is a candidate for the first itinerant antiferromagnet without magnetic constituents. Thermodynamic, transport and susceptibility measurements revealed the magnetic transition at $T_N \simeq 36$ K in TiAu with signatures of antiferromagnetic order such as Curie-Weiss behavior in magnetic susceptibility.

MuSR studies on these systems have been performed in order to: (1) confirm static magnetic order; (2) distinguish whether the transition is second order associated with dynamic critical behavior or first order associated with phase separation between magnetically ordered and paramagnetic volumes; and (3) elucidate distribution of internal field at the muon site to characterize uniformity of the ordered moment size. Comprehensive reports of the present studies on these systems, including synthesis, magnetization, specific heat, neutron scattering, MuSR, and relevant theories, have recently been published in two papers: $(Sc,Lu)_{3.1}In$ in Phys. Rev. X [8] and TiAu in Nature Communications [9]. In this report, we focus on MuSR results highlighting their unique contributions on characterizing static magnetic order and dynamic critical behavior.

## 2.  Research Contents

$Sc_3In$ forms nonstoichiometrically around the ionic ratio Sc:In = 3:1. In the current study, we determined that the optimal composition, which yielded the highest Curie temperature $T_C$ and the paramagnetic moment $\mu_{PM}$, was Sc:In = 3.1:1. Polycrystalline samples of $(Sc_{1-x}Lu_x)_{3.1}In$ ($0 \leq x \leq 0.10$) were prepared by arc-melting Sc, Lu and In. The arc-melted buttons were subsequently annealed over two weeks at temperatures between 700°C and 800°C. The ac susceptibility and dc magnetization measurements were performed in an Arrott-Noakes analysis of critical components of the ferromagnetic transition in $(Sc_{1-x}Lu_x)_{3.1}In$ [8]. Specific heat and low-temperature resistivity measurements revealed the non-Fermi-liquid (NFL) behavior with a possible quantum critical point (QCP) at x = 0.035, which manifested in the logarithmic divergence of the specific heat both in the ferro- and paramagnetic states, as well as the linear temperature dependence of the low-temperature resistivity.

Polycrystalline samples of TiAu were prepared by arc-melting and subsequent annealing. X-ray photo-emission spectroscopy (XPS) was performed on the polished surface of the sample, suggesting that Ti is close to the non-magnetic $4^+$ oxidation state. In DC magnetization the magnetic transition appears as a cusp in the temperature-dependent magnetic susceptibility M(T)/H around 36 K. There was no difference between the field-cooled (FC) and zero-field-cooled (ZFC) M(T)/H curves, which indicates an antiferromagnetic transition, rather than a spin glass freezing. Specific heat show a small peak and the dc resistivity exhibits a drop of about 10% at the Neel temperature $T_N$, which can be ascribed to the loss of spin-disorder scattering. The itinerant nature of the magnetism is confirmed by the following observations: 1) While the inverse susceptibility $H/(M-M_0)$ is linear in temperature up to 800 K showing a Curie-Weiss-like behavior, the paramagnetic moment $\mu_{PM} \sim 0.8$ $\mu_B$ is much larger than the largest measured ordered moment of around 0.01 $\mu_B$;  2) The field-dependent magnetization M(H) does not saturate up to $\mu_0 H = 7$ T;  3) A weak meta-magnetic transition starting around

$\mu_0 H = 3.6$ T for T = 2 K is consistent with the physical picture that the presence of a sharp double peak structure in the electronic density of states (DOS) sufficiently close to the Fermi level resulting in a meta-magnetic transition.   4) The specific heat peak at $T_C$ is too weak and the magnetic entropy Sm is too small for an antiferromagnetic transition of localized moments.

Due to the small saturation moments of itinerant systems, it is not easy to observe static magnetic order of $Sc_3 In$ by neutron diffraction. In contrast, MuSR has a superb sensitivity to small static moments, either having long range order or completely disordered, as MuSR measurements easily detect nuclear dipolar moments that has static moment size of the order of 0.01-0.001 Bohr magnetons with random orientation. Details of the MuSR technique and expected time spectra for various different spin systems can be found in [10], and its previous application to study itinerant-electron magnets can be found in [5]. MuSR measurements of $(Sc_{1-x}Lu_x)_{3.1} In$ were performed at TRIUMF using a He gas flow cryostat at the M20 beam line for the pure x=0 compound and another spectrometer with a dilution fridge cryostat at the M15 beam line for x = 0.01 and x = 0.025 samples. MuSR measurements on TiAu were performed at TRIUMF at M20 (above T = 2 K) and M15 (at T = 0.01-4 K) beamlines.

## 3.  Research results:   (a) $(Sc,Lu)_{3.1} In$

Fig. 5-1(a) shows the MuSR time spectra observed in zero field (ZF) and longitudinal field (LF) at the lowest temperature. The fast relaxation in the early time region in ZF is eliminated by the decoupling effect in a small LF of 100-200 Oe, which indicates that the observed relaxation is due to static magnetic order in all three systems. The ZF time spectra in $Sc_{3.1} In$ were analyzed by assuming a functional form of:

$$G(t) = [A_1 \cos(2\pi v_1 t)e^{-\Lambda_1^2\left(\frac{t^2}{2}\right)} + A_2 \cos(2\pi v_2 t)e^{-\Lambda_2^2\left(\frac{t^2}{2}\right)}$$

$$+(A_{1z} + A_{2z})e^{-\left(\frac{t}{T_1}\right)}V_M + \frac{(1-V_M)\{G_{KT}(t, \Delta_{KT1}) + G_{KT}(t, \Delta_{KT2})\}}{2} \tag{1}$$

where $G_{KT}(t)$ is the Kubo-Toyabe function [11] for random nuclear dipolar fields, $A_1 = A_2$ are presumably due to two magnetically inequivalent muon sites populated with equal probabilities and $A_{1z}$ and $A_{2z}$ are assumed to be half of $A_1$ and $A_2$, respectively, as expected for polycrystalline specimens. The temperature dependence of the two frequencies $v_1$ and $v_2$ is shown in Fig. 5-1(b). The volume fraction $V_M$ of the magnetically ordered region, shown in Fig. 5-1(c), was determined from the amplitudes of the precession signals. $V_M$ decreases gradually with increasing temperature, indicating coexistence of volumes (or regions) with and without static magnetic order. Although the precession signal disappears around T ~ 5.5 K, a small $V_M$ remains above this temperature up to T ≈ 8 K.

The Lu-doped samples show a relaxing signal without precession at low temperatures, indicating a more random internal field, as compared with the undoped $Sc_{3.1} In$.   In order to reproduce the observed line shape, the ZF time spectra of the Lu-doped samples have been analyzed by assuming the following functional form:

$$G(t) = A_1(1-p\sigma^2)e^{\frac{1}{2}\sigma^2 t^2} + \frac{A_1}{2}e^{\frac{t}{T_1}} + A_{bg} \tag{2}$$

where the first term represents the transverse relaxation, the second term is the longitudinal $1/T_1$ component, and the third term is a background signal from the sample holder. The relaxation due to static magnetic order was analyzed with the Kubo-Toyabe function, albeit introducing a phenomenological "dip" parameter p, where smaller p values correspond to line shapes with a shallower dip. Such line shapes are often observed in real materials, including the present case of Lu-doped $Sc_{3.1}In$ systems.

Fig. 5-1(d) shows the doping and temperature dependence of the static internal field, proportional to the ordered moment size, and Fig. 5-1(e) shows the dynamic relaxation rate $1/T_1$ in $(Sc,Lu)_{3.1}In$. No critical behavior is seen in $1/T_1$ of pure $Sc_{3.1}In$ at $T_C$. Together with the gradual evolution of $V_M$, these results in undoped $Sc_{3.1}In$ clearly indicate first-order thermal transition. The reduction of the ordered moment size in Fig. 5-1(d) and the appearance of a small peak of $1/T_1$ in Fig. 5-1(e) seen for the systems with increasing x suggest a minor tendency towards second order criticality when magnetic order is lost with quantum tuning via increasing Lu doping at x ~ 0.035.

## Research results: (b) TiAu

Fig. 5-2(a) and (b) show the MuSR time spectra obtained in TiAu, respectively, in ZF and LF = 100 G. The decoupling of relaxation at low temperatures and the absence of dynamic relaxation around Tc ~ 36 K in LF indicate that the relaxation observed in ZF below T ~ 37 K is due to build-up of static internal field associated with spin freezing. The ZF spectra were analyzed using the Lorentzian Spin Glass (LSG) function [12]:

$$G(t) = V_M \left( \frac{1}{3} + \frac{2}{3} \left( 1-at \right) e^{-at} \right) + (1-V_M) \qquad \textbf{(3)}$$

Shown in Fig. 5-2(c) are the temperature dependence of the relaxation rate *a*, proportional to the static ordered moment size, and the volume fraction $V_M$ of the magnetically ordered regions. MuSR results demonstrate that the static magnetic order occurs in the full volume fraction. Neutron scattering studies in a polycrystalline sample of TiAu detected antiferromagnetic Bragg peak, as shown in Fig. 5-2(d). A small ordered moment size ~ 0.15 Bohr magneton per formula unit was estimated from the Bragg peak intensity. Combination of MuSR and neutron measurements established antiferromagnetic order of TiAu in the entire volume. Absence of $1/T_1$ relaxation in LF-MuSR suggests first-order thermal phase transition reminiscent of results in weak ferromagnets $Sc_{3.1}In$, $(Sr,Ca)RuO_3$ and MnSi.

## 4. Discussions and Conclusions

In conclusion, we studied itinerant electron magnets without constituent magnetic atoms, and demonstrated static ferromagnetic order in $(Sc,Lu)_{3.1}In$ and antiferromagnetic order in TiAu. The thermal phase transition in undoped $Sc_{3.1}In$ and TiAu both showed characteristic features of first-order transition without dynamic critical behavior, consistent with MnSi tuned with hydrostatic pressure [5] and with a theory developed by Belitz, Kirkpatrick and co-workers [3], The reduction of ordered moment size and $T_C$ with increasing $(Sc,Lu)$

substitutions and a moderate peaking of $1/T_1$ in Lu doped systems hint possible trends towards second order quantum criticality. This behavior might be related to a recent theoretical work [13] which predicts recovery of second order critical behavior due to disorder. Further experiments are required, however, to elucidate the role of disorder.

The ZF-MuSR time spectra in TiAu exhibit fast damping without clear precession signal, resembling those observed in spin glass systems. At a glance, it is not easy to reconcile this feature with the observation of Bragg peak in neutron scattering which indicates long range spatial spin correlations. However, similar trend has been observed by MuSR and neutron scattering in $(Sr_{1.5}Ca_{0.5})RuO_4$ [5,14]. We shall remind here that if the ordered moment size has a wide spatial distribution, even a long-range ordered spin system will acquire highly inhomogeneous internal field distribution for MuSR and other local probes. In neutron scattering, however, spatial randomness superimposed on long-range order will generate diffuse scattering signal (in addition to Bragg peaks) spread in a wide region of momentum space, which is practically invisible. This provides one possible explanation for the simultaneous observation of a relatively sharp Bragg peak by neutrons and a highly damped MuSR time spectra in TiAu. Further experiments are required, however, for detailed determination of spatial spin correlations.

## Acknowledgements

## References

[1] Stoner, E. C. Collective electron ferromagnetism. *Proceedings of the Royal Society of London A* **165**, 372-414 (1938).

[2] Moriya, T., *et al.* Effect of spin fluctuations on itinerant electron ferromagnetism. *Journal of Physical Society of Japan* **34**, 639-651 (1973).

[3] Belitz, T., *et al.* Tricritical Behavior in Itinerant Quantum Ferromagnets. *Physical Review Letters* **94**, 247205 (2005).

[4] Lohneysen, H. v., *et al.* Fermi-liquid instabilities at magnetic quantum phase transitions. *Reviews of Modern Physics* **79**, 1015 (2007).

[5] Uemura, Y. J., *et al.* Phase separation and suppression of critical dynamics at quantum phase transitions of MnSi and $(Sr_{1-x}Ca_x)RuO_3$. *Nature Physics* **3**, 29-35 (2007).

[6] Matthias, B. T., *et al.* Ferromagnetism in solid solutions of Scandium and Indium. *Physical Review Letters* **7**, 7-9 (1961) .

[7] Mattias, B. T., *et al.* Ferromagnetism of a Zirconium-Zinc compound. *Physical Review* **109**, 604-605 (1958).

[8] Svanidze, E., *et al.* Non-Fermi Liquid Behavior Close to a Quantum Critical Point in a

Ferromagnetic State without Local Moments. *Physical Review X* **5**, 011026 (2015).

[9] Svanidze, E., *et al.* An Itinerant Antiferromagnetic Metal without Magnetic Constituents. *Nature Communication*, **6**, 7701 (2015).

[10] Uemura, Y.J., µSR Relaxation Functions in Magnetic Materials, in *Muon Science*, ed. by S.L. Lee, S.H. Kilcoyne, R. Cywinski, Institute of Physics Publishing, London, 1999, pp. 85-114.

[11] Hayano, R. S., *et al.* Zero- and Low- Field Spin Relaxation Studied by Positive Muons. *Physical Review B* **20**, 850 (1979).

[12] Uemura, Y.J., *et al.*, Muon Spin Relaxation in AuFe and CuMn Spin Glasses, *Physical Review B* **31**, 546-563 (1985).

[13] Sang, Y., Belitz, D., and Kirkpatrick, T.R., Disorder dependence of the ferromagnetic quantum phase transition, *Physical Review Letters* **113**, 207201 (2014).

[14] Kunkemöller, S., et al., Spin-density-wave ordering in $Ca_{0.5}Sr_{1.5}RuO_4$ studied by neutron scattering, *Physical Review B* **89**, 045119 (2014).
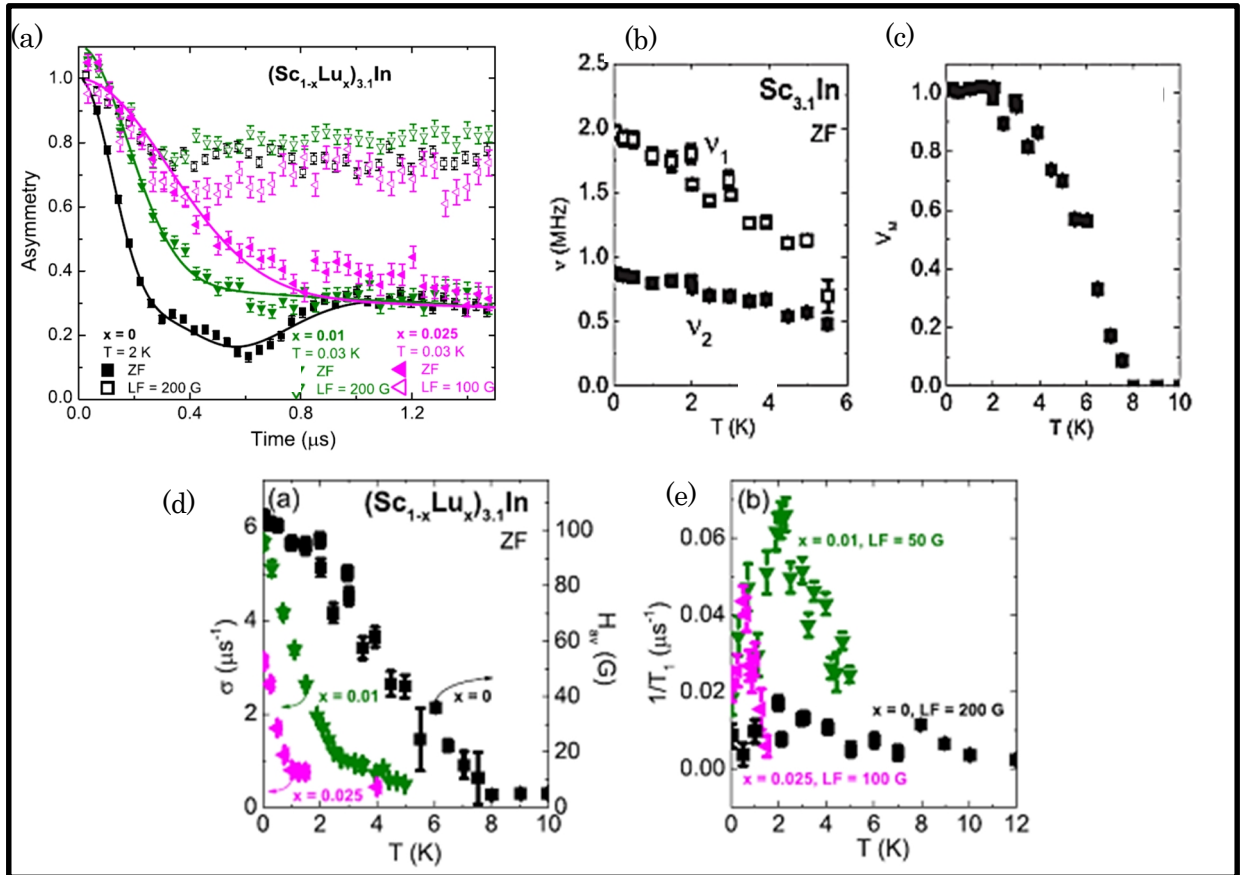
Fig. 5-1: MuSR results on $(Sc_{1-x}Lu_x)_{3.1}In$ (from [8]). (a) The time spectra of ZF-MuSR and LF-MuSR (with LF = 100 – 200 G) at T = 2 K for x = 0 and T = 0.03 K for x = 0.01 and 0.025. The solid lines represent fits to Eq. (1) for x = 0 and Eq. (2) for x = 0.01 and 0.025. (b) The two frequencies observed in ZF in the undoped x = 0 compound. (c) The volume fraction $V_M$

of the magnetically ordered regions in the x=0 compound. (d) The static relaxation rate σ in the x = 0.01 and 0.025 compounds (left vertical axis) and the static field strength in the x = 0 compound (right vertical axis). The scale of the two vertical axes is set to allow direct comparisons of the sizes of the static ordered moments. (e) The dynamic muon spin relaxation rate $1/T_1$ measured in LF = 200 G for x = 0, 50 G for x = 0.01 and 100 G for x = 0.025 compounds.

TiAu
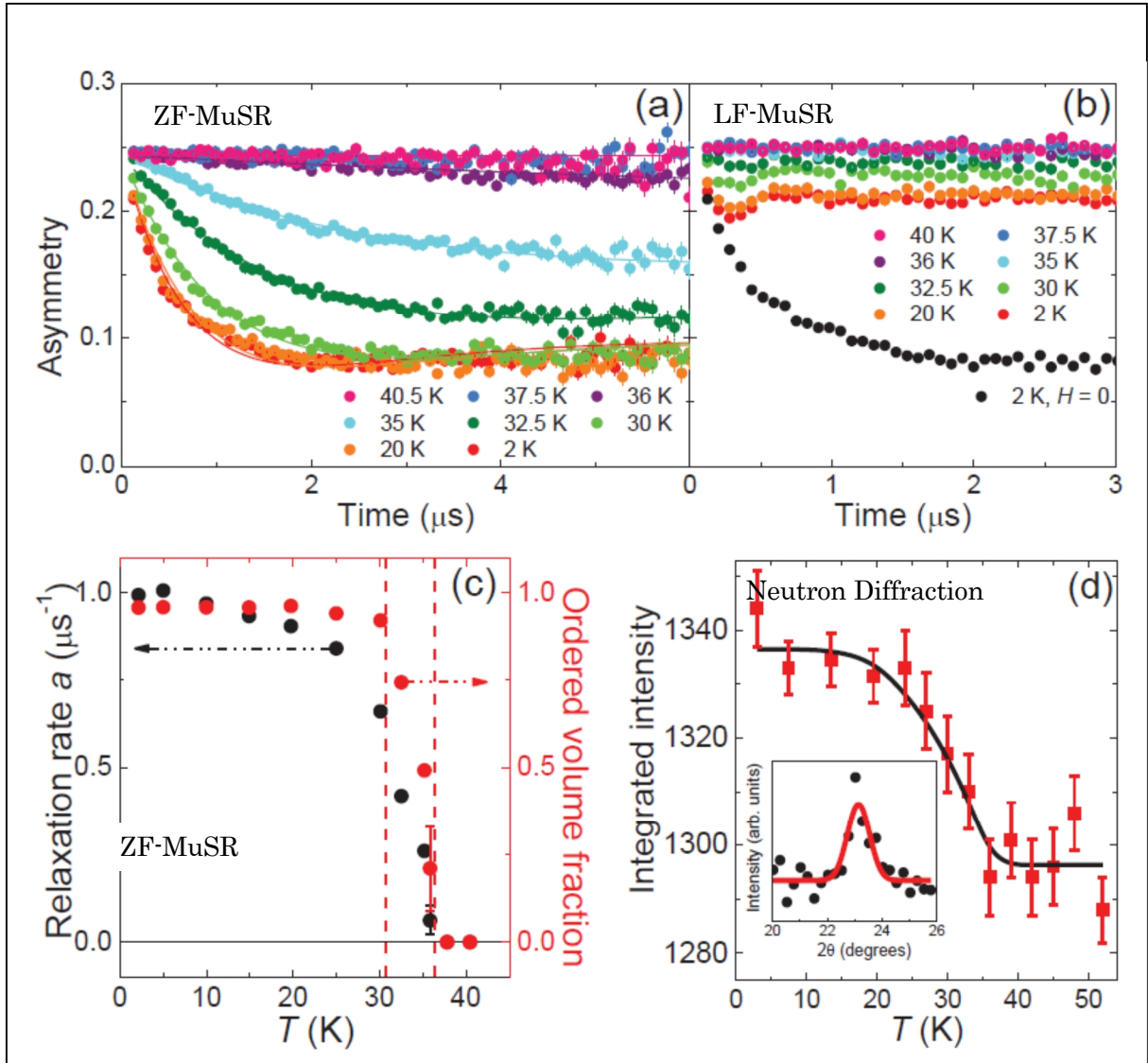


Fig. 5-2: MuSR and neutron diffraction results on TiAu (from [9]). MuSR time spectra (a) in H = 0, with solid lines represensing fits with Eq. 3, and (b) in LF = 100 G. The application of small LF eliminates the relaxation response. For comparison, the H = 0 T = 2 K asymmetry is shown in black circles. (c) MuSR relaxation rate a (black circles, left) and volume fraction $V_M$ (red circles, right) in ZF as a function temperature. (d) Neutron scattering results on polycrystalline specimen of TiAu. Integrated intensity of the $(0, \pi/b, 0)$ magnetic Bragg peak is shown as a function of temperature with mean-field fit ($T_N$ = 36.2 K, black curve). Inset: net counts normalized for 2 min. counting time between 2.5 K and 60 K, showing the $(0, \pi/b, 0)$ magnetic Bragg peak fit with a resolution-limited Gaussian (red line). Uncertainties are statistical in origin and represent one standard deviation.

# 6. Study on specific behavior of anthropogenic radionuclides at solid solution interface

Bernd Grambow[1], Tomo Suzuki-Mursan[1], Ali Traboulsi[1], Johan Vandenborre[1],

F. Haddad[2], Guillaume Blain[1], Massoud Fattahi[1]

Toshi Ohnuki[3], Naofumi Kozai[3], Fuminori Sakamoto[3], Qianqian Yu[3], and Takumi Saito[3]

Norihiko Nishiguchi[4] (Hokkaido U.) , Tamotsu Kozaki[4], Naoko Watanabe[4], Satoshi Utsunomiya[5] (Kyushu U.), Shota Masaki[5], Osamu Shira[6] (Kyoto U.), Takayuki Sasaki[7], Kenji Nanba[8] (Fukushima U.)

[1]SUBATECH, UMR 6457, Ecole des Mines de Nantes, CNRS/IN2P3, Université de Nantes, France
[2]ARRONAX cyclotron − 1, France
[3] Advanced Science Research Center, Japan Atomic Energy Agency, Japan
[4] Faculty of Engineering, Hokkaido University, Japan
[5] Department of Chemistry, Kyushu University, Japan
[6] School of Bioscience, Tokyo University of Technology, Japan
[7] Graduate School of Agriculture, [8] Graduate School of Engineering, Kyoto University, Japan
[9] Faculty of Symbiotic Systems Science, Fukushima University, Japan

Abstract

We investigated the reactions proceeded at the interface between solid and solution under the outside stimulus of irradiation or nano-particles. For the effects of irradiation, the corrosion of $UO_2$ was studied in the presence of Cs. We found that regardless the irradiation atmosphere, the grain boundaries are much more degraded than the intact $UO_2$ grains, and formed studite. In the presence of CaCl the quantity of U species is released by corrosion of the material surface. The formation of $UO_3 \cdot nH_2O$ oxide layer inhibits the production of $H_2$, indicating that oxides layer formation plays a role of protective one. For the effects of nano-particles, effect of $CeO_2$ alternative of $UO_2$ on the response of yeast was studied. The yeast released organic matter into the NaCl solution at all pH values. Some organic species released from the yeast are expressed or suppressed after exposure to CeNPs. Although the cytotoxicity is not caused by CeNPs, a glycolysis enzyme, ENO2, was expressed in the intracellular protein after exposure to CeNPs. These results suggest that irradiation and environmental nanoparticles affect the interaction of solid-solution, which potentially exert influence on the mobility of elements in the surrounding environment.

## 1. Research objectives

Anthropogenic radionuclides (AR) have been generated in nuclear power plants, reprocessing facility, and nuclear weapons tests. The radiotoxicity of the ARs that were generated by the nuclear fission of uranium and plutonium atoms during reactor operation affects long-duration in the environment.

In the environment ARs react with solid phase in soil and rock during migration in surface water. The solid phases contain minerals (inorganic material), degraded organic matter and microorganisms. The ARs change their chemical species at the interface between water and these solids. One of the reactions is adsorption on the solid, and the adsorption changes chemical species of ARs from dissolved one to insoluble ones. Unfortunately, the solid phases are not stable in the long-term, but changed with time by physical and chemical interaction with water. For instance, minerals are dissolved and precipitated to form secondary minerals It is question on how ARs behave during the change of a primary solid phase to a secondary one, whether initially solid-bound ARs become mobilized into the surface water or become incorporated in the secondary solid phase, and how the chemical speciation of the ARs change during these transformations. These reactions proceed under dynamic conditions, and the chemical species on the secondary solid cannot be estimated from studying the interaction of ARs with this solid phase under a static condition. The specific behavior of ARs at the interface between solid and water during the alteration should be occurred. However, the specific behavior of ARs during the alteration is not understood.

Therefore, the objective of the research is to find a new specific behavior of ARs at the interface between solid and water during the alteration.

## 2. Research content

In ARs, cesium ($^{137}$Cs) is one the most important radionuclides to consider in safety assessment due to its strong thermal power component and high radiotoxicity in a nuclear spent fuel and its presence as a volatile gas in the corium [1]. In a previous work, the radiolytic corrosion of $UO_2$ by $^4He^{2+}$ radiolysis of water at the solid-liquid interface has been investigated [2]. The aim of this investigation was to determine the effect of certain parameters, which vary in realistic conditions, on the $UO_2$ corrosion. Interesting parameters studied were the influence of the absorbed dose and the irradiation atmosphere on the oxidation of $UO_2$, and the impact of the oxide layer on the surface reactivity. However, in the present work, the originality consisted in investigating together the different faces of the chemistry under irradiation of the Cs-$UO_2$-water interface by coupling for the first time (1) characterization of the secondary oxidized phases formed on the solid surface, (2) determination of the radiolytic yields of $H_2O_2$ and $H_2$ produced by water radiolysis and (3) quantification of soluble uranium released into the solution by corrosion of the material.

The $UO_2$ precipitates may interact with microorganisms. When size of the $UO_2$ precipitates is

small as much as nano-particles, a new specific behavior of $UO_2$ nano-particles and microbial response may be observed. The various effects of nanoparticles on microorganisms have been previously studied [3,4]. The adherence of nanoparticles to the cell membranes of microorganisms can alter the fluidity of cell surfaces [5]. So, we have conducted the study on the interaction of $CeO_2$ (surrogate of $UO_2$) nano-particles and yeast *Saccharomyces serevisiae*.

## 3. Research Results

$UO_2$-TRISO particles in contact with water were oxidized under $He^{2+}$ irradiation. Cesium (CsCl Aldrich 99.9%, $2\times10^{-3}$ $mol \cdot L^{-1}$) was added after irradiation. The experiments were performed in open to air and closed with air atmospheres (Fig. 6-1). $He^{2+}$ irradiation was realized by the $He^{2+}$ beam of the ARRONAX cyclotron with energy of 66.5 MeV and a dose rate of 4.4 $kGy \cdot min^{-1}$. The dose rate was determined *in situ* (during irradiation) by Fricke dosimetry [6].

The surface of the solid was characterized by Raman spectroscopy during and after irradiation in order to follow any temporal evolution of its corrosion/oxidation process. $H_2O_2$ and $H_2$ were measured by UV-VIS spectrophotometry with triiodide method [7] and micro Gas Chromatography ($\mu$-GC), respectively. Solution aliquots taken from irradiated samples were filtrated at 45 $\mu$m in order to exclude colloidal particles and acidified with 2% distilled nitric acid. Uranium and cesium were analyzed by inductively coupled plasma mass spectrometry (ICP-MS Quadripolaire Xseries 2, THERMOELECTRON).
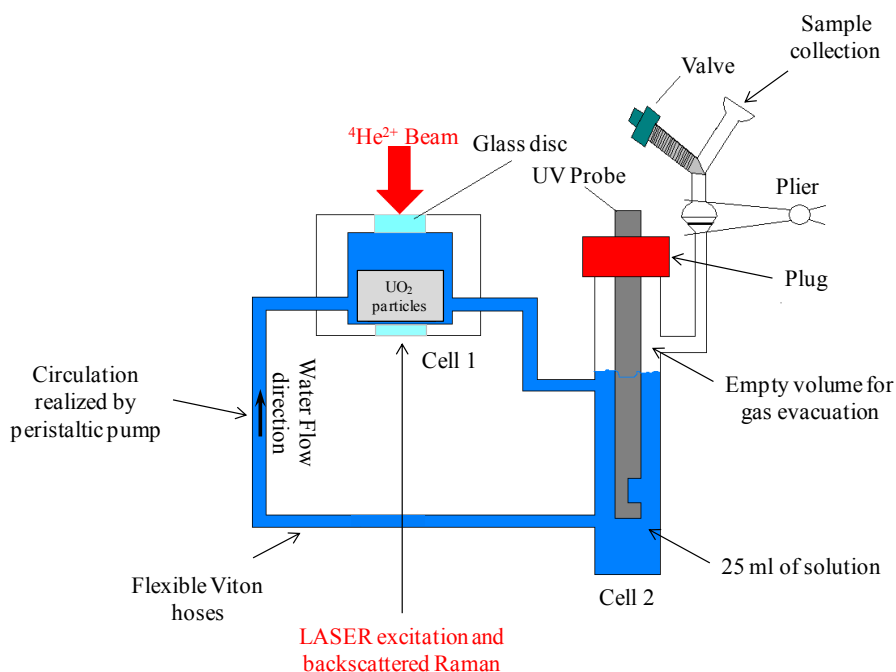


Fig. 6-1: Irradiation cell disposal, and sample collection for gas analysis

UO$_2$ TRISO particle is constituted of UO$_2$ based kernel (500 μm of diameter) composed by grains and grain boundaries (Fig. 6-2). The grain size has been measured between 10 and 20 μm. After irradiation, SEM pictures were realized on the surface particles in order to determine the zones most affected by the corrosion process (Fig. 6-3). Fig. 6-3 clearly shows that regardless the irradiation atmosphere, the grain boundaries are much more degraded than the UO$_2$ grains. It appears that the corrosion did not occur homogeneously on the entire surface. Some regions of the grains surface are indeed more corroded. This result was checked by Raman mapping spectroscopy on these surfaces and, then, the corrosion can be considered as localized on grain boundary [8].
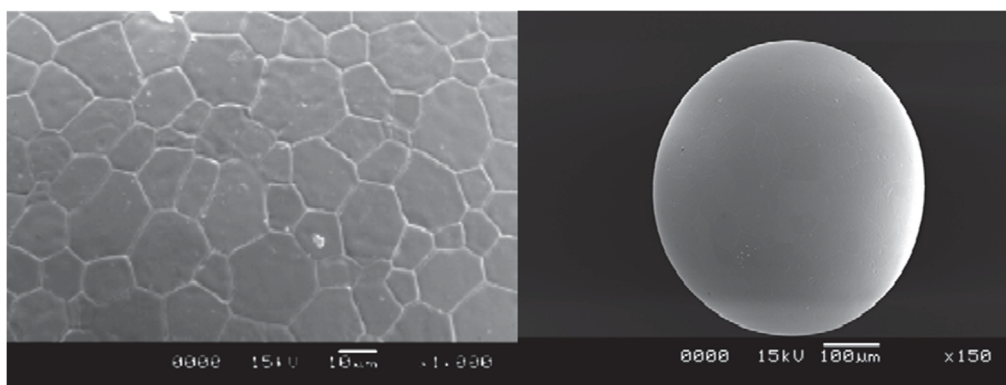


Fig. 6-2: SEM picture of the surface of unirradiated UO$_2$ particle
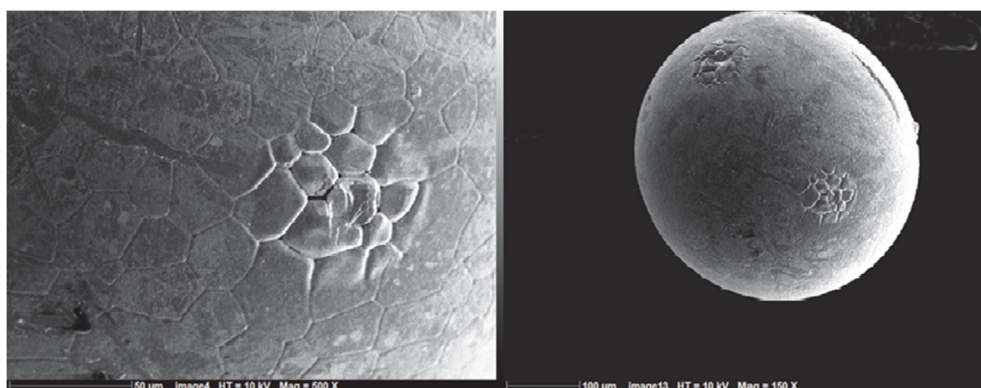


Fig. 6-3: SEM pictures of the surface of UO$_2$ particle corroded in open to air atmosphere

Surface characterization by Raman spectroscopy showed that He$^{2+}$ irradiation of water in contact with UO$_2$ induced oxidation of its surface and this oxidation depended on the irradiation conditions. The results below are obtained for two samples irradiated at a dose of 8.73 kGy in open to air and closed with air atmospheres. Fig.6-4 shows the Raman spectra of unirradiated UO$_2$ (a) and a sample irradiated in open atmosphere (b, c, d). The spectra of the irradiated sample are obtained 0.3, 42 and 169 hours after contact with the irradiated water. When comparing the two spectra, 2 identical Raman signals at 445 and 560 cm$^{-1}$ are detected.

The first one characterizes the U-O stretch in the fluorite structure of $UO_2$ and the second one indicates the presence of defects in the matrix. After irradiation, two Raman signals appear at 820 and 865 cm$^{-1}$ indicating the formation of studtite ($UO_4$ 4($H_2O$)). The detected studtite is formed by oxidation of the $UO_2$ surface by $H_2O_2$ produced by water radiolysis and not by $O_2$ present in the air (see Eq.1).

$$UO_2 + 2H_2O_2 \rightarrow UO_2(O_2)(H_2O)_2 \tag{1}$$

$H_2O_2$ produced by water radiolysis in this experiment is measured with a$G(H_2O_2)$ value equal to 0.06 µmol·J$^{-1}$ about two-fold lower than in ultra pure water without $UO_2$ solid [6].

After irradiation, cesium is added in solution and $UO_2$ surface is probed by Raman spectroscopy (Fig.6-5). No U/Cs phase is detected at surface. Moreover, after the addition of cesium, the Raman signals at 820 and 865 cm$^{-1}$ of the studtite are not observed and the concentration of uranium in solution increase by 2-orders of magnitude. The presence of chloride (Cl-) brought during the addition of Cs may have reacted with the surface of $UO_2$. Solution is irradiated in pure water and the addition of chloride may have changed the ionic force from 0 to 0.002 mol·L$^{-1}$.
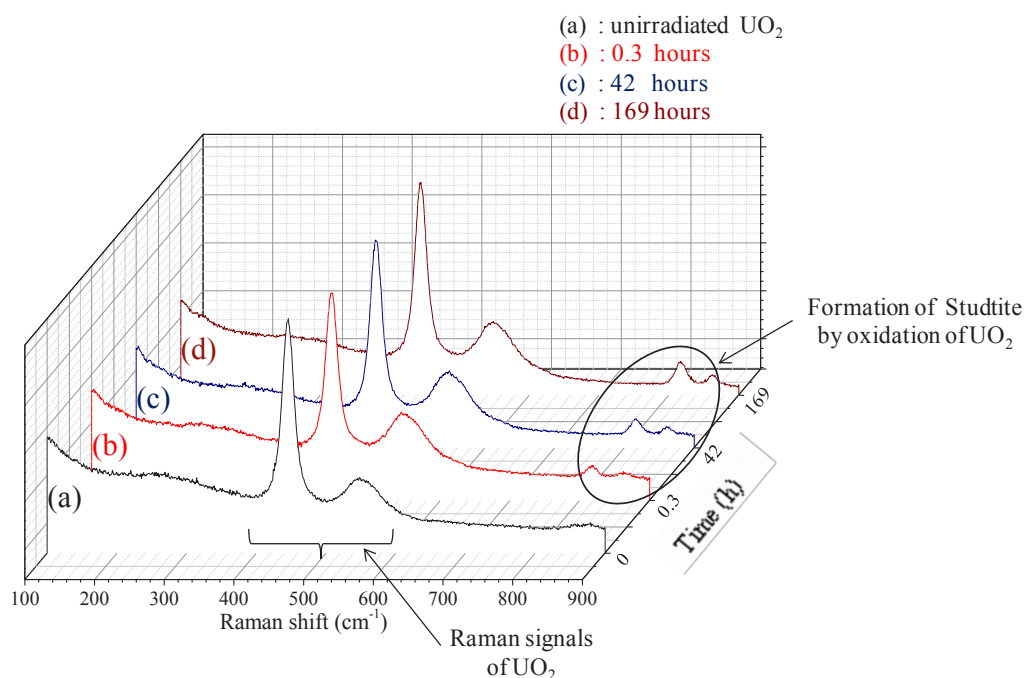


Fig. 6-4: Raman spectra of unirradiated $UO_2$ ((a)) and a sample irradiated at 8.73 kGy under open atmosphere ((b), (c) and (d)). The spectra (b), (c) and (d) are obtained 0.3, 42 and 169 hours after contact with the irradiated solution.
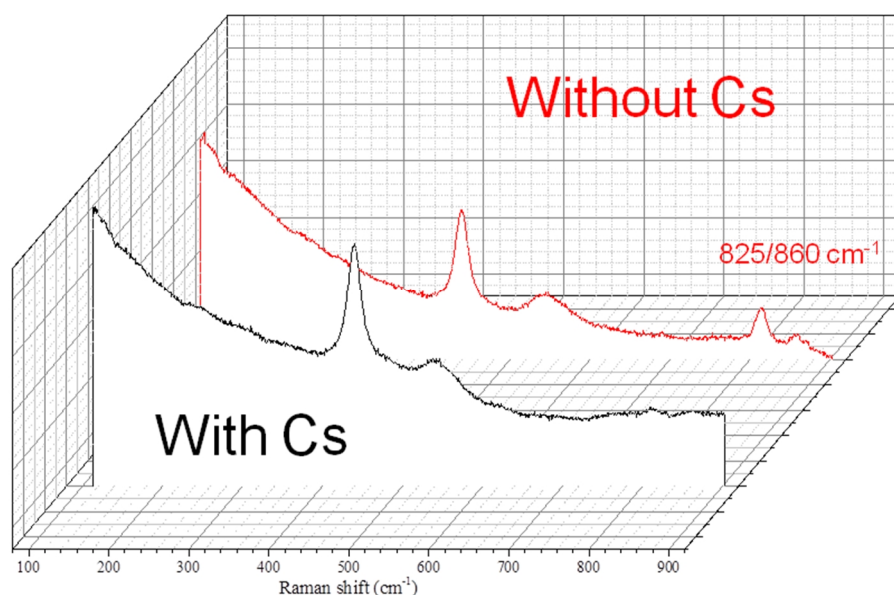
Fig. 6-5: Raman spectra of irradiated $UO_2$ at 8.73 kGy under open atmosphere in absence and presence of cesium ($2\times10^{-3}$ mol·$L^{-1}$)

The knowledge of the surface state is important to understand the surface reactivity notably when the solid phase contents redox sensitive elements such as uranium which can be easily oxidized. To assess the surface reactivity, $UO_2$ particles were partially oxidized by hydrogen peroxide to produce a $UO_3.nH_2O$ layer, a common alteration product formed by $UO_2$ oxidation (Fig. 6-6). The oxidized uranium spheres were placed in a device with a 1 mol·$L^{-1}$ NaCl solution to keep the humidity close to 100%. Hence, the water available for radiolysis corresponds to a few layers adsorbed on the oxidation product of the 50 $UO_2$ particles. In order to simulate the alpha decay of actinides the 68 MeV, alpha beam has been degraded until 6 MeV through a titanium sheet which thickness was estimated by the Monte Carlo SRIM calculations [9,10]. Hydrogen produced after irradiation showed that the quantity of hydrogen produced in presence of oxidized $UO_2$ is in the same order of magnitude to that of blank (= absence of $UO_2$ particles). It is clearly shown that no further hydrogen was produced in the presence of oxidized $UO_2$ spheres. Regarding to the previous experiments, a complementary experiments would be the addition of CsCl in irradiated solution in presence of $UO_3.nH_2O$ oxide layer in order to assess the influence of CsCl on the dissolution or not of this oxide layer which here acts as a protective layer.
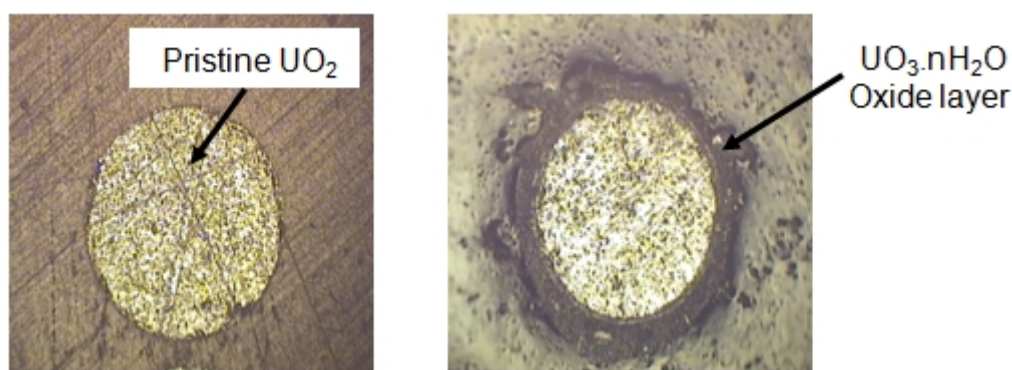
Fig. 6-6: surface oxidation of UO₂ particles for alpha irradiation experiments

For the study of interaction of CeO2 nano-particles with microbes, synthetic CeNP was purchased from Strem Chemicals, Inc., Newburyport, MA, USA (#58-1400, <7 nm). The size and morphology were analyzed using a high-resolution transmission electron microscope (HRTEM; JEOL ARM200F) equipped with energy dispersive X-ray spectroscopy (EDS) at an acceleration voltage of 200 kV. *Saccharomyces cerevisiae* X-2180 was used as microorganism. *Saccharomyces cerevisiae* X-2180 was grown in 150 mL of sterilized YPD medium containing 10 g $L^{-1}$ yeast extract, 20 g $L^{-1}$ peptone, and 20 g $L^{-1}$ dextrose, labeled as "non-CeNP yeast". *Saccharomyces cerevisiae* X-2180 grown in 150 mL of sterilized YPD medium containing 250 mg $L^{-1}$ CeNPs was labeled as "CeNP yeast". The yeast was incubated for 18 h on a rotary shaker at 120 revolutions per minute (rpm) at 25 ± 1 °C. The cells were separated from the suspension through centrifugation for 10 min at 5000 rpm and washed three times with 1 mmol $L^{-1}$ NaCl solution.

The cytotoxicity assessment of yeast exposed to CeNPs was performed on yeast incubated in YPD media and yeast exposed to CeNP in solution. The growth curves for yeast incubated in media with or without CeNPs showed that there is no cytotoxicity of the CeNPs during incubation in the medium.

Fig. 6-7 shows the HPLC chromatogram of the DOM released from non-CeNP and CeNP yeast at pH 3, 5, and 7, revealing significant differences in the relative amounts of released organic species. Peak intensity typically reflects the amount of organic matter with the same retention time because the molar absorbance coefficient is defined by the functional group, and peaks with same retention time typically correspond to the same species. Thus, the observed changes in HPLC peak intensity indicate changes in the amount of organic matter released from CeNP yeast. Notably, the single peaks in the HPLC chromatogram potentially but can be extracted at a specific retention time depending on the column conditions. The amount of the organic species eluted at 25.42 min was higher for CeNP yeast than that for non-CeNP yeast at pH values from 3 to 5. The gradual increase in the peak at 25.42 min with decreasing pH, even in the absence of CeNP, indicates that the organic species associated with this peak were released through acidic stress and exposure to CeNPs. At pH 3, seven organic species with

peaks at 18.61, 19.61, 20.20, 30.37, 31.67, 34.30, and 36.60 min decreased for the CeNP yeast, while at pH 5 and 7, only four species (peaks at 20.20, 30.37, 31.67, and 34.30 min) were slightly decreased. This indicates that the exposure of yeast to CeNPs changed the relative amounts of the released organic species in similar manner at all pH conditions; acidity only slightly modified the relative amounts of organic species.

The HPLC-ESI-IT-TOF-MS analyses of organic matters released after contact with CeNPs revealed a significant change in the relative amount of the organic species after exposure to CeNPs. It is also noted that the majority of the organic matter in the released substances have low molecular masses with m/z<1000. Hence, the alterations in microbial metabolism caused by exposure to CeNPs possibly reflect changes in intracellular enzymes.
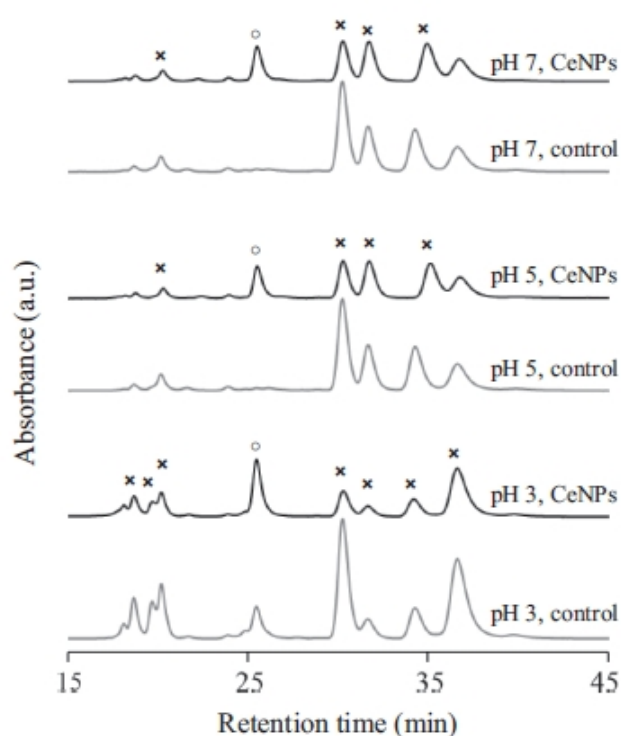


Fig. 6-7 HPLC separation of organicmatter released to the yeast exposure solution. Gray line (control): organic matter released from non-CeNP yeast. Black line: organic matter released from CeNP yeast. Circle and cross symbols stand for the amounts of increase and decrease in organic species, respectively, after exposure to CeNPs. In solutions at pH 5 and 7, the peak at the retention time of 34 min was shifted slightly backward, reflecting a change in the eluent at that time; this did not affect the analysis.

CCB-R250-stained 2-D gel electrophoresis patterns of intracellular proteins from the cell lysates of yeast grown in CeNP-free medium and CeNP medium showed that The proteins of Eno2p and Rps24bp were released. Eno2p is a protein involved in the glycolytic system, and this enzyme typically catalyzes the hydrolysis of 2-phosphoglyceric acid as follows:

$$2\text{-phosphoglycerate} \rightleftharpoons \text{phosphoenolpyruvate} + H_2O$$

4. Conclusions

This work brings some light on the radiolytic corrosion of $UO_2$ by investigating the different faces of its chemistry under irradiation. Surface reactivity of $UO_2$ is affected by the absence or presence of an oxide layer at surface. In absence of oxide layer, (1) secondary phase is formed on the solid surface, (2) $H_2$ plays a role as an inhibitor agent, (3) $H_2O_2$ plays a role as oxidative agent, and (4) the quantity of U species released by corrosion of the material surface influenced by the presence of CsCl. In presence of oxide layer, $H_2$ is not produced and $UO_3.nH_2O$ oxide layer plays a role of protective layer.

We investigated the effects of $CeO_2$ nanoparticles on microbial metabolites released from yeast based on laboratory based experiment, in which the yeast harvested from a medium containing 0-250 ppm of CeNPs was incubated for 120 h in a 1 mM NaCl solution at pHs 2, 3, 5, and 7. The yeast released organic matter, P, K, and Mg into the NaCl solution at all pH values. The released P comprised ~80% orthophosphate and 20% organically bound phosphate. Some organic species released from the yeast are expressed or suppressed after exposure to CeNPs. Although the cytotoxicity is not caused by CeNPs, a glycolysis enzyme, ENO2, was expressed in the intracellular protein after exposure to CeNPs. These results suggest that environmental nanoparticles affect microbial metabolism and change the dominant species of the released substances, which potentially exert influence on the mobility of elements in the surrounding environment.

Acknowledgements

References

[1] Y. Pontillon, G.r. Ducros, P.P. Malgouyres, Nuclear Engineering and Design, **240**, 1843-1852 (2010).

[2] A. Traboulsi, J. Vandenborre, G. Blain, B. Humbert, J. Barbet, M. Fattahi, J. Phys. Chem. C, **118**, 1071-1080 (2014).

[3] Yamamoto, A., Honma, R., Sumita, M., Hanawa, T., Cytotoxicity evaluation of ceramic particles of different sizes and shapes. J. Biomed. Mater. Res. 68A (2), 244–256 (2004).

[4] Pelletier, D.A., Suresh, A.K., Holton, G.A., McKeown, C.K.,Wang,W., Gu, B.,Mortensen, N.P., Allison, D.P., Joy, D.C., Allison,M.R., Brown, S.D., Phelps, T.J., Doktycz,M.J., Effects of engineered cerium oxide nanoparticles on bacterial growth and viability, Applied and Environmental Microbiology, 76(24), 7981–7989 (2010).

[5] Schwegmann, H., Feitz, A.J., Frimmel, F.H., Influence of the zeta potential on the sorption and toxicity of iron oxide nanoparticles on S. cerevisiae and E. coli. J. Colloid Interface Sci. 347 (1), 43–48 (2010).

[6] H. Fricke, E.J. Hart, Chemical Dosimetry, Radiation Dosimetry, Academic Press, New York, USA, (1966).

[7] J.A. Ghormley, C.J. Hochanadel, J. Am. Chem. Soc., 76, 3351-3352 (1954).

[8] A. Traboulsi, J. Vandenborre, G. Blain, J. Barbet, M. Fattahi, Impact of water radiolysis on uranium dioxide corrosion, in: 7th EC FP CP FIRST-Nuclides, 2nd Annual Workshop 2013, Antwerpen, Belgium, (2013).

[9] F. Crumière, Etudes de l'effet des rayonnements ionisants sur l'eau : Rendements radiolytiques de l'hydrogène moléculaire, in: Ph.D., Université de Nantes, Nantes (2012).

[10] J.F. Ziegler, J.P. Biersack, U. Littmark, The Stopping and Range of Ions in Matter, Pergamon Press, New York, USA (1985).

# 7. f電子系化合物におけるスピン・軌道・フェルミ面のゆらぎ

# と量子臨界現象

青木 大[1,2]、神戸 振作[3]、ジャック・フルケ[2]
Dai Aoki[1,2], Shinsaku Kambe[2] and Jacques Flouquet[3]

[1] 東北大学金属材料研究所
IMR, Tohoku University
[2] INAC/SPSMS, CEA-Grenoble
[3] 日本原子力研究開発機構 先端基礎研究センター
Advanced Science Research Center, Japan Atomic Energy Agency

## 概要

　ウラン化合物の 5f 電子は遍歴と局在の中間的な性質を示し、スピン軌道相互作用も大きいことから、多彩で魅力的な物性を示す。その顕著な例が、強磁性超伝導や非自明な秩序と共存する超伝導など、非従来型の超伝導である。これは、強磁性秩序、多極子秩序の量子臨界現象などと密接に関連し、その発現機構に注目が集まっている。本研究では、スピン、軌道、フェルミ面のゆらぎをキーワードにこれらの多彩な量子現象の解明を目指した。とくに URhGe のリエントラント超伝導について、フェルミ面のゆらぎ、強磁性スピンゆらぎの観点から、純良単結晶を用いた精密物性測定を行い、強磁性超伝導の新奇な知見が得られた。強磁性超伝導以外でも多数の試料育成、物性測定を行なった。

## 1. 研究目的

　5f 電子を含むアクチノイド化合物は物性物理の宝庫である。強磁性と超伝導の共存、「高温」超伝導、隠れた秩序、多極子秩序など多彩で魅力的な現象が知られている。たとえば、強磁性超伝導はウラン化合物でしか知られておらず、スピン三重項が担う磁場誘起超伝導など、その特徴は際立っている。これは物性を担う 5f 電子が局在と遍歴の中間的な性質持ち、なおかつ強いスピン・軌道相互作用を伴うからだと考えられる。一方、アクチノイド化合物は放射性物質であるために、取り扱いが難しく現在国内で十分な量の試料育成が行なえる研究所は、原子力機構先端研と東北大金研の二カ所のみである。

　本研究の目的はまず（1）アクチノイド化合物における新物質開発と新奇超伝導体の探索。そして（2）縦の磁気ゆらぎによる高い超伝導臨界磁場、横の磁気ゆらぎによる高い超伝導転移温度の発現機構の微視的測定手段による解明、およびその指針に基づいた物質開発である。

　エネルギー問題が重要な課題となる中、優れた特性を持つ新たな超伝導物質の探索は、応用面からもきわめて重要である。そのためには、新物質開発とともに高い超伝導転移温度、高い臨界磁場の発現機構を基礎研究の立場から解明することが待ち望まれている。とくに、アクチノイド化合物は比較的純良な試料が得られるために、温度、磁場、圧力などの外部パラメータで物質を磁気不安定点近傍にチューニングして精密測定を行う上で格好の舞台となる。このような視点からアクチノ

イド研究が行われた例はあまりなく、しかも実際に出来る施設は限られている。本研究の独創性・特色はこの点にある。本研究は、原子力機構先端研、東北大金研大洗センターを研究拠点とし、国際的な研究協力としてフランス原子力庁 CEA-Grenoble も本研究課題に参画した。

## 2．研究内容

　継続研究として、前年度に得られた成果をもとに、これを発展させる研究を行なう計画を立てた。前年度、得られた主な成果を挙げると（a)URhGe-Co 置換による NMR 信号の観測と「メタ磁性」（spin reorientation）近傍における縦揺らぎの発散的増大の観測、(b)URhGe、UCoGe におけるフェルミ面の不安定性の観測、(c)URu2Si2 および関連物質おける強磁場下における磁気構造の決定,(d)UCoAl におけるホール効果および熱電能測定による強磁性量子臨界現象の研究などである。これらの成果をもとに、H26 年度は具体的に以下の研究を中心にすすめる計画を立てた。

（1）アクチノイド化合物における新物質開発と純良単結晶育成
　前年度に引き続き、新物質開発と純良単結晶育成を行なう。東北大金研では、フラックス法、ブリッジマン法、チョクラルスキー法、気相成長法による純良単結晶育成が行なえる体制が整った。また、育成された試料を迅速に評価するための X 線、電気抵抗、比熱といった基礎物性測定の装置開発も進んでいる。CEA-Grenoble においては、新たにウラン化合物のフラックス法による単結晶育成が最近出来るようになった。すでに USn$_3$ の単結晶育成に成功している。これらの地道な努力を継続して新物質開発を行なっていく。
　新物質を開発する上で重要となるのは、その指針である。ジグザグチェーン、カゴ状などの特徴的な結晶構造、適度なウラン間距離、低い磁気秩序温度、大きな電子比熱係数などを考慮しながら開発を進める。とくにジグザグチェーンに関しては、ウランサイトにおける局所的な反転対称性の欠如と強いスピン軌道相互作用のもとでのパリティ混成、これらの状況下での新奇量子相が理論的に示唆されている。実際、強磁性超伝導体の UGe$_2$、URhGe、UCoGe は全て結晶構造にジグザグチェーンがある。かつて我々が URhGe の強磁性超伝導の発見したのも、ジグザグチェーンの結晶構造が念頭にあったからである。
　育成された試料は、組成の確認、結晶構造の決定が重要である。先端研の試料育成のメンバーの協力を得て、EPMA、X 線単結晶構造解析による試料の同定を行う。

（2）ウラン強磁性超伝導体 UGe$_2$,UCoGe,URhGe の磁場誘起超伝導および強磁性量子臨界現象の研究
　強磁性と超伝導が微視的に共存する系はウラン化合物 UGe$_2$、URhGe、UCoGe の三種類である。これらは青木が純良単結晶育成に成功し、長年研究を行ってきた物質である。いずれの物質も超伝導転移温度は 1K 以下と低いにもかかわらず、通常の BCS 型超伝導から期待される値より数十倍も高い上部臨界磁場 H$_{c2}$ を持つ。さらに、いずれの物質も磁場再突入（リエントラント）型あるいは S 字型の H$_{c2}$ 相図を示す。電気抵抗、比熱、磁化測定などのマクロ測定から、強磁性の Ising 型の縦の磁気ゆらぎによって増強されたスピン三重項の平行スピン対が超伝導を担っていると考えられる。また、前年度の成果として遍歴メタ磁性体 UCoAl の強磁性量子臨界現象の研究が進んでいる。常圧で磁場を上げて行くと常磁性から磁場誘起強磁性の１次のメタ磁性を示すが、臨界終点温度 T$_{CEP}$ よりも上の高温ではクロスオーバーである。臨界終点では磁気的な揺らぎが発達し、T$_1$、比熱、熱電能、ホール係数等に大きな異常が現れる。圧力を加えると T$_{CEP}$ を 0 K にチューニング可能で

あり、その量子臨界終点近傍ではシャープな有効質量の増大と新しい量子相の出現が示唆されている。これらは、フェルミ面の不安定性および揺らぎの異方性の問題とも絡んできわめて興味深い。強磁性量子臨界現象は強磁性超伝導体の磁場誘起超伝導相とも関連があり、これらを統一的に理解することが重要である。

本研究では、NMR、ドハース・ファンアルフェン効果によるフェルミ面の観測、熱電能測定、中性子散乱実験などの実験手段を用いて強磁性超伝導の磁場誘起相および強磁性量子臨界現象を調べる。とくに、$T_1$ の測定によるスピンゆらぎの異方性、フェルミ面の直接観測による対称性の破れとトポロジーによる新量子相、磁気励起と異方的超伝導ギャップの形成などについて注目する。

　UCoGe、URhGe において RRR=100 を越える純良単結晶育成に成功しているが、いまだ観測されているフェルミ面は一部である。また、UCoAl については RRR=20 以下であり、量子振動の観測にはいたっていない。さらなる純良単結晶育成と測定精度の向上により、フェルミ面を決定したい。

　東北大金研では、精密二軸回転機構付き NMR 装置（神戸グループ、金研設置済み）、ドハース効果用トップローディング型希釈冷凍機（先端研所有、金研設置済み）、15T 超伝導マグネット（金研、現有設備）を利用する。このため液体ヘリウム購入代が必要である。ドハース効果をさらに高精度に測定するための装置の整備も行う。

　CEA-Grenoble では、新トップローディング型希釈冷凍機（CEA、現有設備）による 10mK までのドハース効果、LNCMI（強磁場研）での 35T までの NMR およびドハース効果測定、ILL での非弾性中性子散乱実験を予定している。得られた結果は、随時、バンド計算と比較し理論との比較・解釈を試みる。

（３）反強磁性 XY 型ゆらぎによる超伝導発現機構と超伝導転移温度の解明
　アクチノイド化合物とくに超ウラン化合物の超伝導転移温度は高く、重い電子系超伝導（Ce の
4f 電子系）と銅酸化物高温超伝導（d 電子系）の間をつなぐものと考えられている。超伝導体の統一的理解のためにアクチノイド化合物超伝導は重要な位置を占めている。上述のように強磁性超伝導体の場合、Ising 型のゆらぎが高い $H_{c2}$ を持つ超伝導と関連していると考えられるが、反強磁性の XY 型の横ゆらぎが超伝導転移温度と関係しており、これを NMR などの微視的測定手段により解明する。NMR グループとの密接な研究協力をすすめる。また、得られた知見を指針として新たな「高温」超伝導体を探索する。NMR 測定装置は上述の先端研所有、金研設置済みの装置



図 7-1:URhGe の温度−磁場相図（参考文献５）

を利用する。必要に応じて、ILL での非弾性中性子散乱実験、大型放射光施設 ESRF や SPring8 での共鳴 X 線散乱実験も行なう。
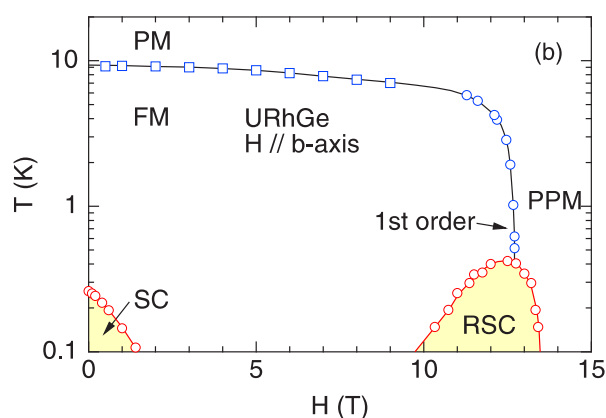
## 3. 研究結果

参考文献にあるように、成果を論文として多数発表することができた。この内、フェルミ面の揺らぎと超伝導の関係について解説したい。URhGe は、9.5K にキュリー温度を持つ強磁性体である。TiNiSi 型斜方晶の結晶構造を持ち、U 原子が a 軸方向にジグザグチェーンを形成する。磁化容易軸は c 軸方向である。図 7-1 に示すように、磁化困難軸の b 軸方向に磁場を加えると、キュリー温度は磁場増大とともに減少する。ゼロ磁場では、強磁性と共存する超伝導が 0.25K で発現し、約 2T の上部臨界磁場 Hc2 を示す。驚くべきことに、キュリー温度が減少し 0K に向かう近傍の強磁場中で超伝導が再び現れ、リエントラント型の超伝導相が現れる。その転移温度は 12T で 0.4K と、ゼロ磁場の 0.25K よりも高く、磁場によって超伝導が安定化していることが分かる。強磁性と共存する超伝導であること、高い磁場でも超伝導が安定化することから、URhGe の超伝導は平行スピン対によるスピン三重項超伝導が実現している可能性が高い。この超伝導の発現機構を明らかにすることはきわめて重要である。本研究では、URhGe の純良単結晶を育成し、極低温・強磁場下で磁場方向を精密制御しながらホール効果を測定した[5]。これにより、リエントラント超伝導近傍におけるフェルミ面の不安定性について調べた。図 7-2 に磁場を b 軸方向に加えたときのホール抵抗の磁場依存性を示す。リエントラント超伝導の前後でホール抵抗の傾きが大きく変化していることが分かる。URhGe のホール効果は正常ホール効果と異常ホール効果の 2 つの寄与から成り立っている。異常ホール効果の寄与を注意深く差し引くことで、リエントラント超伝導前後で正常ホール効果が符号反転を伴う大きな変化を示すことが分かった。単純なシングルバンドモデルで考えると、URhGe のフェルミ面が大きく変化し、キャリア数が変化していることを示している。強磁性超伝導は、UCoGe の NMR の実験から、強磁性の縦のスピン揺らぎが重要な役割を果たしていることが分かっていた。本研究は、それに加えてフェルミ面の揺らぎも超伝導の安定化に重要であることを明らかにした。この研究は、NMR による URhGe の強磁性ゆらぎの直接観測の研究にもつながった[17]。URhGe に Co を 10% ドープした系において、キュリー温度がゼロに向かう spin reorientatio 磁場でスピンースピン緩和率 T2 が発散的に増大することを見出した。強磁性量子臨界点と量子臨界終点近傍で、縦の磁気ゆらぎが発散的に増大することを示している。
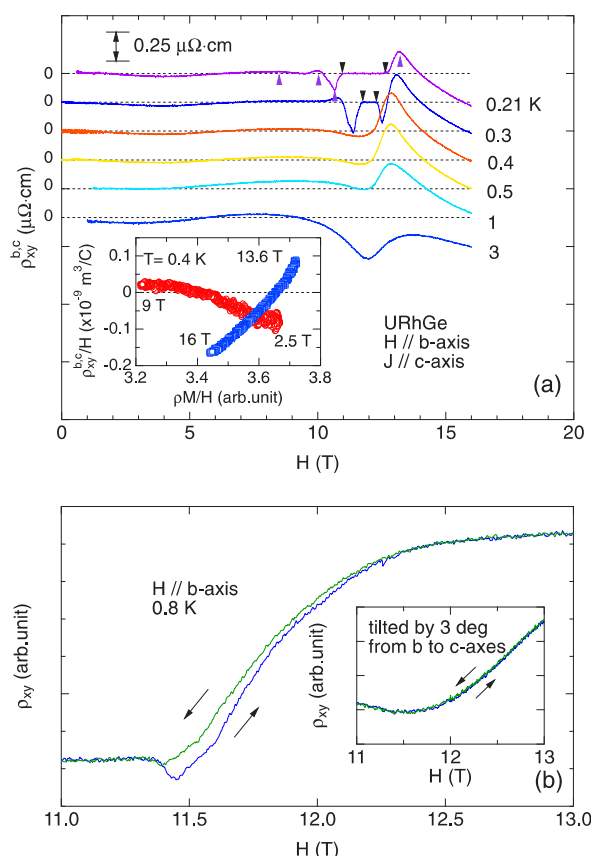


図 7-2:URhGe のホール効果の磁場依存性
（参考文献５）

## 4. まとめ

強磁性超伝導体を中心に様々なウラン・希土類化合物の純良単結晶育成に成功し、スピンゆらぎ、

フェルミ面のゆらぎの観点から精密物性測定を行った。純良単結晶育成と新物質探索は、物性物理学における要であり、ウランを含む f 電子系化合物はその意味で宝の山である。今後、ジグザグ構造など、特徴ある結晶構造をヒントにした物質開発を精力的に行いたい。バルクに限らず、薄膜や微細加工など現代的な手法による物質開発にも取り組みたい。

## 参考文献

[1] G. W. Scheerer, W. Knafo, D. Aoki, M. Nardone, A. Zitouni, J. Beard, J. Billette, J. Barata, C. Jaudet, M. Suleiman, P. Frings, L. Drigo, A. Audouard, T. D. Matsuda, A. Pourret, G. Knebel, and J. Flouquet: Phys. Rev. B **89**, 165107 (2014).

[2] D. Aoki and J. Flouquet: J. Phys. Soc. Jpn. **83**, 061011 (2014).

[3] Y. Tokunaga, T. Nishi, M. Nakada, A. Itoh, H. Sakai, S. Kambe, Y. Homma, F. Honda, D. Aoki, R. E. Walstedt: Phys. Rev. B **89**, 214416 (2014).

[4] D. Aoki, A. Gourgout, A. Pourret, G. Bastien, G. Knebel, J. Flouquet: C. R. Physique **15**, 630 (2014).

[5] D. Aoki, G. Knebel, J. Flouquet: J. Phys. Soc. Jpn. **83**, 094719 (2014).

[6] D. J. Hykel, C. Paulsen, D. Aoki, J. R. Kirtley, and K. Hasselbach: Phys. Rev. B **90**, 184501 (2014).

[7] M. Taupin, L. Howald, D. Aoki, and J.-P. Brison: Phys. Rev. B 90 180501R (2014).

[8] J. Buhot, M.-A. Méasson, Y. Gallais, M. Cazayous, A. Sacuto, G. Lapertot, D. Aoki: Phys. Rev. Lett. **113**, 266405 (2014).

[9] Y. Shimizu, B. Salce, T. Combier, D. Aoki, J. Flouquet: J. Phys. Soc. Jpn. 84, 023704 (2015).

[10] S. Araki, M. Hayashida, N. Nishiumi, H. Manabe, Y. Ikeda, T. C. Kobayashi, K. Murata, Y. Piotr Wiśniewski, D. Aoki, Y. Onuki, E. Yamamoto, Y. Haga: J. Phys. Soc. Jpn. **84**, 024705 (2015).

[11] D. Aoki, F. Honda, Y. Homma, D.X. Li, R. Settai, H. Harima, Y. Onuki: J. Phys. Soc. Jpn. **84**, 035002 (2015).

[12] J. Buhot, M. A. Méasson, Y. Gallais, M. Cazayous, A. Sacuto, F. Bourdarot, S. Raymond, G. Lapertot, D. Aoki, L. P. Regnault, A. Ivanov, P. Piekarz, K. Parlinski, D. Legut, C. C. Homes, P. Lejay, R. P. S. M. Lobo: Phys. Rev. B **91**, 035129 (2015).

[13] M. Boukahil, A. Pourret, G. Knebel, D. Aoki, Y. Onuki, J. Flouquet: Phys. Rev. B **90**, 075127 (2014).

[14] Pourret, D. Aoki, M. Boukahil, J. P. Brison, W. Knafo, G. Knebel, S. Raymond, M. Taupin, Y. Onuki, J. Flouquet: J. Phys. Soc. Jpn. **83**, 061002 (2014).

[15] S. Raymond, S. M. Ramos, D. Aoki, G. Knebel, V. P. Mineev, G. Lapertot: J. Phys. Soc. Jpn. **83**, 013707(2014).

[16] M. Taupin, L. Howald, D. Aoki, J. Flouquet, J. P. Brison: Phys. Rev. B **89**, 041108 (2014).

[17] Y. Tokunaga, D. Aoki, H. Mayaffre, S. Kramer, M.-H. Julien, C. Berthier, M. Horvatic, H. Sakai, S. Kambe and S. Araki: Phys. Rev. Lett. **114**, 216401, (2015).

# 国際単位系（SI）

## 表1．SI 基本単位

| 基本量 | SI 基本単位 名称 | 記号 |
|---|---|---|
| 長　　　　さ | メートル | m |
| 質　　　　量 | キログラム | kg |
| 時　　　　間 | 秒 | s |
| 電　　　　流 | アンペア | A |
| 熱力学温度 | ケルビン | K |
| 物　質　量 | モル | mol |
| 光　　　　度 | カンデラ | cd |

## 表2．基本単位を用いて表されるSI組立単位の例

| 組立量 | SI 組立単位 名称 | 記号 |
|---|---|---|
| 面　　　　積 | 平方メートル | $m^2$ |
| 体　　　　積 | 立方メートル | $m^3$ |
| 速　さ，速　度 | メートル毎秒 | m/s |
| 加　　速　　度 | メートル毎秒毎秒 | $m/s^2$ |
| 波　　　　数 | 毎メートル | $m^{-1}$ |
| 密度，質量密度 | キログラム毎立方メートル | $kg/m^3$ |
| 面　積　密　度 | キログラム毎平方メートル | $kg/m^2$ |
| 比　　体　　積 | 立方メートル毎キログラム | $m^3/kg$ |
| 電　流　密　度 | アンペア毎平方メートル | $A/m^2$ |
| 磁　界　の　強　さ | アンペア毎メートル | A/m |
| 量濃度[(a)]，濃度 | モル毎立方メートル | $mol/m^3$ |
| 質　量　濃　度 | キログラム毎立方メートル | $kg/m^3$ |
| 輝　　　　度 | カンデラ毎平方メートル | $cd/m^2$ |
| 屈　折　率[(b)] | （数字の）1 | 1 |
| 比　透　磁　率[(b)] | （数字の）1 | 1 |

(a) 量濃度（amount concentration）は臨床化学の分野では物質濃度（substance concentration）ともよばれる。
(b) これらは無次元量あるいは次元1をもつ量であるが、そのことを表す単位記号である数字の1は通常は表記しない。

## 表3．固有の名称と記号で表されるSI組立単位

| 組立量 | SI 組立単位 名称 | 記号 | 他のSI単位による表し方 | SI基本単位による表し方 |
|---|---|---|---|---|
| 平　　面　　角 | ラジアン[(b)] | rad | 1[(b)] | m/m |
| 立　　体　　角 | ステラジアン[(b)] | sr[(c)] | 1[(b)] | $m^2/m^2$ |
| 周　　波　　数 | ヘルツ[(d)] | Hz | | $s^{-1}$ |
| 力 | ニュートン | N | | $m\ kg\ s^{-2}$ |
| 圧　力，応　力 | パスカル | Pa | $N/m^2$ | $m^{-1}\ kg\ s^{-2}$ |
| エネルギー，仕事，熱量 | ジュール | J | N m | $m^2\ kg\ s^{-2}$ |
| 仕事率，工率，放射束 | ワット | W | J/s | $m^2\ kg\ s^{-3}$ |
| 電荷，電気量 | クーロン | C | | s A |
| 電位差（電圧），起電力 | ボルト | V | W/A | $m^2\ kg\ s^{-3}\ A^{-1}$ |
| 静　電　容　量 | ファラド | F | C/V | $m^{-2}\ kg^{-1}\ s^4\ A^2$ |
| 電　気　抵　抗 | オーム | Ω | V/A | $m^2\ kg\ s^{-3}\ A^{-2}$ |
| コンダクタンス | ジーメンス | S | A/V | $m^{-2}\ kg^{-1}\ s^3\ A^2$ |
| 磁　　　　束 | ウエーバ | Wb | Vs | $m^2\ kg\ s^{-2}\ A^{-1}$ |
| 磁　束　密　度 | テスラ | T | $Wb/m^2$ | $kg\ s^{-2}\ A^{-1}$ |
| インダクタンス | ヘンリー | H | Wb/A | $m^2\ kg\ s^{-2}\ A^{-2}$ |
| セルシウス温度 | セルシウス度[(e)] | ℃ | | K |
| 光　　　　束 | ルーメン | lm | cd sr[(c)] | cd |
| 照　　　　度 | ルクス | lx | $lm/m^2$ | $m^{-2}\ cd$ |
| 放射性核種の放射能[(f)] | ベクレル[(d)] | Bq | | $s^{-1}$ |
| 吸収線量, 比エネルギー分与, カーマ | グレイ | Gy | J/kg | $m^2\ s^{-2}$ |
| 線量当量, 周辺線量当量, 方向性線量当量, 個人線量当量 | シーベルト[(g)] | Sv | J/kg | $m^2\ s^{-2}$ |
| 酸　素　活　性 | カタール | kat | | $s^{-1}\ mol$ |

(a)SI接頭語は固有の名称と記号を持つ組立単位と組み合わせても使用できる。しかし接頭語を付けた単位はもはやコヒーレントではない。
(b)ラジアンとステラジアンは数字の1に対する単位の特別な名称で、量についての情報をつたえるために使われる。実際には、使用する時には記号rad及びsrが用いられるが、習慣として組立単位としての記号である数字の1は明示されない。
(c)測光学ではステラジアンという名称と記号srを単位の表し方の中に、そのまま維持している。
(d)ヘルツは周期現象についてのみ、ベクレルは放射性核種の統計的過程についてのみ使用される。
(e)セルシウス度はケルビンの特別な名称で、セルシウス温度を表すために使用される。セルシウス度とケルビンの単位の大きさは同一である。したがって、温度差や温度間隔を表す数値はどちらの単位で表しても同じである。
(f)放射性核種の放射能（activity referred to a radionuclide）は、しばしば誤った用語で"radioactivity"と記される。
(g)単位シーベルト（PV,2002,70,205）についてはCIPM勧告2（CI-2002）を参照。

## 表4．単位の中に固有の名称と記号を含むSI組立単位の例

| 組立量 | SI 組立単位 名称 | 記号 | SI 基本単位による表し方 |
|---|---|---|---|
| 粘　　　　度 | パスカル秒 | Pa s | $m^{-1}\ kg\ s^{-1}$ |
| 力のモーメント | ニュートンメートル | N m | $m^2\ kg\ s^{-2}$ |
| 表　面　張　力 | ニュートン毎メートル | N/m | $kg\ s^{-2}$ |
| 角　　速　　度 | ラジアン毎秒 | rad/s | $m\ m^{-1}\ s^{-1}=s^{-1}$ |
| 角　加　速　度 | ラジアン毎秒毎秒 | $rad/s^2$ | $m\ m^{-1}\ s^{-2}=s^{-2}$ |
| 熱流密度, 放射照度 | ワット毎平方メートル | $W/m^2$ | $kg\ s^{-3}$ |
| 熱容量, エントロピー | ジュール毎ケルビン | J/K | $m^2\ kg\ s^{-2}\ K^{-1}$ |
| 比熱容量, 比エントロピー | ジュール毎キログラム毎ケルビン | J/(kg K) | $m^2\ s^{-2}\ K^{-1}$ |
| 比エネルギー | ジュール毎キログラム | J/kg | $m^2\ s^{-2}$ |
| 熱伝導率 | ワット毎メートル毎ケルビン | W/(m K) | $m\ kg\ s^{-3}\ K^{-1}$ |
| 体積エネルギー | ジュール毎立方メートル | $J/m^3$ | $m^{-1}\ kg\ s^{-2}$ |
| 電　界　の　強　さ | ボルト毎メートル | V/m | $m\ kg\ s^{-3}\ A^{-1}$ |
| 電　荷　密　度 | クーロン毎立方メートル | $C/m^3$ | $m^{-3}\ s\ A$ |
| 表　面　電　荷 | クーロン毎平方メートル | $C/m^2$ | $m^{-2}\ s\ A$ |
| 電束密度, 電気変位 | クーロン毎平方メートル | $C/m^2$ | $m^{-2}\ s\ A$ |
| 誘　　電　　率 | ファラド毎メートル | F/m | $m^{-3}\ kg^{-1}\ s^4\ A^2$ |
| 透　　磁　　率 | ヘンリー毎メートル | H/m | $m\ kg\ s^{-2}\ A^{-2}$ |
| モルエネルギー | ジュール毎モル | J/mol | $m^2\ kg\ s^{-2}\ mol^{-1}$ |
| モルエントロピー, モル熱容量 | ジュール毎モル毎ケルビン | J/(mol K) | $m^2\ kg\ s^{-2}\ K^{-1}\ mol^{-1}$ |
| 照射線量（X線及びγ線） | クーロン毎キログラム | C/kg | $kg^{-1}\ s\ A$ |
| 吸　収　線　量　率 | グレイ毎秒 | Gy/s | $m^2\ s^{-3}$ |
| 放　射　強　度 | ワット毎ステラジアン | W/sr | $m^4\ m^{-2}\ kg\ s^{-3}=m^2\ kg\ s^{-3}$ |
| 放　射　輝　度 | ワット毎平方メートル毎ステラジアン | $W/(m^2\ sr)$ | $m^2\ m^{-2}\ kg\ s^{-3}=kg\ s^{-3}$ |
| 酵素活性濃度 | カタール毎立方メートル | $kat/m^3$ | $m^{-3}\ s^{-1}\ mol$ |

## 表5．SI 接頭語

| 乗数 | 名称 | 記号 | 乗数 | 名称 | 記号 |
|---|---|---|---|---|---|
| $10^{24}$ | ヨ　タ | Y | $10^{-1}$ | デ　シ | d |
| $10^{21}$ | ゼ　タ | Z | $10^{-2}$ | セ　ン　チ | c |
| $10^{18}$ | エ　ク　サ | E | $10^{-3}$ | ミ　リ | m |
| $10^{15}$ | ペ　タ | P | $10^{-6}$ | マイクロ | μ |
| $10^{12}$ | テ　ラ | T | $10^{-9}$ | ナ　ノ | n |
| $10^{9}$ | ギ　ガ | G | $10^{-12}$ | ピ　コ | p |
| $10^{6}$ | メ　ガ | M | $10^{-15}$ | フェムト | f |
| $10^{3}$ | キ　ロ | k | $10^{-18}$ | ア　ト | a |
| $10^{2}$ | ヘ　ク　ト | h | $10^{-21}$ | ゼ　プ　ト | z |
| $10^{1}$ | デ　カ | da | $10^{-24}$ | ヨ　ク　ト | y |

## 表6．SIに属さないが、SIと併用される単位

| 名称 | 記号 | SI 単位による値 |
|---|---|---|
| 分 | min | 1 min=60 s |
| 時 | h | 1 h =60 min=3600 s |
| 日 | d | 1 d=24 h=86 400 s |
| 度 | ° | 1°=($\pi$/180) rad |
| 分 | ’ | 1’=(1/60)°=($\pi$/10 800) rad |
| 秒 | ” | 1”=(1/60)’=($\pi$/648 000) rad |
| ヘクタール | ha | 1 ha=1 $hm^2$=$10^4 m^2$ |
| リットル | L, l | 1 L=1 l=1 $dm^3$=$10^3 cm^3$=$10^{-3} m^3$ |
| トン | t | 1 t=$10^3$ kg |

## 表7．SIに属さないが、SIと併用される単位で、SI単位で表される数値が実験的に得られるもの

| 名称 | 記号 | SI 単位で表される数値 |
|---|---|---|
| 電　子　ボ　ル　ト | eV | 1 eV=1.602 176 53(14)×$10^{-19}$J |
| ダ　ル　ト　ン | Da | 1 Da=1.660 538 86(28)×$10^{-27}$kg |
| 統一原子質量単位 | u | 1 u=1 Da |
| 天　文　単　位 | ua | 1 ua=1.495 978 706 91(6)×$10^{11}$m |

## 表8．SIに属さないが、SIと併用されるその他の単位

| 名称 | 記号 | SI 単位で表される数値 |
|---|---|---|
| バ　ー　ル | bar | 1 bar=0.1MPa=100 kPa=$10^5$Pa |
| 水銀柱ミリメートル | mmHg | 1 mmHg≈133.322Pa |
| オングストローム | Å | 1 Å=0.1nm=100pm=$10^{-10}$m |
| 海　　　里 | M | 1 M=1852m |
| バ　ー　ン | b | 1 b=100$fm^2$=($10^{-12}$cm$)^2$=$10^{-28} m^2$ |
| ノ　ッ　ト | kn | 1 kn=(1852/3600)m/s |
| ネ　ー　パ | Np | } SI単位との数値的な関係は、対数量の定義に依存。 |
| ベ　ル | B | |
| デ　シ　ベ　ル | dB | |

## 表9．固有の名称をもつCGS組立単位

| 名称 | 記号 | SI 単位で表される数値 |
|---|---|---|
| エ　ル　グ | erg | 1 erg=$10^{-7}$ J |
| ダ　イ　ン | dyn | 1 dyn=$10^{-5}$N |
| ポ　ア　ズ | P | 1 P=1 dyn s cm$^{-2}$=0.1Pa s |
| ストークス | St | 1 St=1$cm^2$ s$^{-1}$=$10^{-4} m^2$ s$^{-1}$ |
| スチルブ | sb | 1 sb=1cd cm$^{-2}$=$10^4$cd m$^{-2}$ |
| フォト | ph | 1 ph=1cd sr cm$^{-2}$=$10^4$lx |
| ガ　ル | Gal | 1 Gal =1cm s$^{-2}$=$10^{-2}$ms$^{-2}$ |
| マクスウエル | Mx | 1 Mx = 1G $cm^2$=$10^{-8}$Wb |
| ガ　ウ　ス | G | 1 G =1Mx cm$^{-2}$=$10^{-4}$T |
| エルステッド[(a)] | Oe | 1 Oe ≙ ($10^3$/4$\pi$)A m$^{-1}$ |

(a) 3元系のCGS単位系とSIでは直接比較できないため、等号「 ≙ 」は対応関係を示すものである。

## 表10．SIに属さないその他の単位の例

| 名称 | 記号 | SI 単位で表される数値 |
|---|---|---|
| キ　ュ　リ　ー | Ci | 1 Ci=3.7×$10^{10}$Bq |
| レ　ン　ト　ゲ　ン | R | 1 R = 2.58×$10^{-4}$C/kg |
| ラ　ド | rad | 1 rad=1cGy=$10^{-2}$Gy |
| レ　ム | rem | 1 rem=1 cSv=$10^{-2}$Sv |
| ガ　ン　マ | γ | 1 γ=1 nT=$10^{-9}$T |
| フェルミ | | 1 フェルミ=1 fm=$10^{-15}$m |
| メートル系カラット | | 1 メートル系カラット = 0.2 g =2×$10^{-4}$kg |
| ト　ル | Torr | 1 Torr = (101 325/760) Pa |
| 標　準　大　気　圧 | atm | 1 atm = 101 325 Pa |
| カ　ロ　リ　ー | cal | 1 cal=4.1858J（「15℃」カロリー），4.1868J（「IT」カロリー），4.184J（「熱化学」カロリー） |
| ミ　ク　ロ　ン | μ | 1 μ =1μm=$10^{-6}$m |

(第8版，2006年)